

Second-order regression models exhibit progressive sharpening to the edge of stability

Anonymous Authors¹

Abstract

Recent studies of gradient descent with large step sizes have shown that there is often a regime with an initial increase in the largest eigenvalue of the loss Hessian (progressive sharpening), followed by a stabilization of the eigenvalue near the maximum value which allows convergence (edge of stability). These phenomena are intrinsically non-linear and do not happen for models in the constant Neural Tangent Kernel (NTK) regime, for which the predictive function is approximately linear in the parameters. As such, we consider the next simplest class of predictive models, namely those that are quadratic in the parameters, which we call second-order regression models. For quadratic objectives in two dimensions, we prove that this second-order regression model exhibits progressive sharpening of the NTK eigenvalue towards a value that differs slightly from the edge of stability, which we explicitly compute. In higher dimensions, the model generically shows similar behavior, even without the specific structure of a neural network, suggesting that progressive sharpening and edge-of-stability behavior aren't unique features of neural networks, and could be a more general property of discrete learning algorithms in high-dimensional non-linear models.

1. Introduction

A recent trend in the theoretical understanding of deep learning has focused on the *linearized* regime, where the Neural Tangent Kernel (NTK) controls the learning dynamics (Jacot et al., 2018; Lee et al., 2019). The NTK describes learning dynamics of all networks over short enough time horizons, and can describe the dynamics of wide networks over large time horizons. In the NTK regime, there is a function-space

¹Anonymous Institution, Anonymous City, Anonymous Region, Anonymous Country. Correspondence to: Anonymous Author <anon.email@domain.com>.

Preliminary work. Under review by the International Conference on Machine Learning (ICML). Do not distribute.

ODE which allows for explicit characterization of the network outputs (Jacot et al., 2018; Lee et al., 2019; Yang, 2021). This approach has been used across the board to gain insights into wide neural networks, but it suffers a major limitation: the model is linear in the parameters, so it describes a regime with relatively trivial dynamics that cannot capture feature learning and cannot accurately represent the types of complex training phenomena often observed in practice.

While other large-width scaling regimes can preserve some non-linearity and allow for certain types of feature learning (Bordelon & Pehlevan, 2022; Yang et al., 2022), such approaches tend to focus on the small learning-rate or continuous-time dynamics. In contrast, recent empirical work has highlighted a number of important phenomena arising from the non-linear discrete dynamics in training practical networks with large learning rates (Neyshabur et al., 2017; Gilmer et al., 2022; Ghorbani et al., 2019; Foret et al., 2022). In particular, many experiments have shown the tendency for networks to display *progressive sharpening* of the curvature towards the *edge of stability*, in which the maximum eigenvalue of the loss Hessian increases over the course of training until it stabilizes at a value equal to roughly two divided by the learning rate, corresponding to the largest eigenvalue for which gradient descent would converge in a quadratic potential (Wu et al., 2018; Giladi et al., 2020; Cohen et al., 2022a;b).

In order to build a better understanding of this behavior, we introduce a class of *quadratic regression models* which display all the relevant phenomenology yet are simple enough to admit numerical and analytic understanding. Models of this type have been investigated previously in order to understand other phenomena that occur beyond the NTK regime (Zhu et al., 2022a; Roberts et al., 2022). In a particular low-dimensional setting, we prove that the maximum NTK eigenvalue converges to (near) the edge of stability, and we demonstrate empirically that progressive sharpening to the edge of stability occurs *generically* in the large datapoint, large model limit. Finally, we conduct a numerical analysis on the properties of a real neural network and use tools from our theoretical analysis to show that edge-of-stability behavior “in the wild” shows some of the same patterns as the theoretical models.

055 **1.1. Concurrent work**

056 Several concurrent works have investigated similar questions
057 about edge of stability and have developed insights
058 that nicely complement the conclusions we develop here.

059
060 **Zhu et al. (2022b)** propose a minimalist model in the form
061 of a degree-4 function (or degree-8 objective) and prove that
062 sharpness converges to a value close to, but not equal to,
063 the edge of stability. While these results are similar to our
064 results in the low-dimensional setting, we find that edge-of-
065 stability behavior can occur for degree-2 functions, and that
066 the final sharpness differs from the convergence threshold
067 by a precise problem-dependent amount which we calculate.

068
069 **Damian et al. (2022)** develop an explanatory model for
070 stabilization of sharpness near the edge of stability based on
071 the nonlinear self-interaction of the top eigenmode of the
072 Hessian as well as its effective interaction with the other
073 eigenmodes. The low-dimensional dynamics capture the full
074 behavior over short timescales when the sharpness is near
075 the stability threshold, and closely resemble the differential
076 equations we develop in the low-dimensional limit of our
077 model. Our setup is somewhat less general, as it is restricted
078 to quadratic models, but it affords us some additional in-
079 sights beyond what was possible in **Damian et al. (2022)**. In
080 particular, we are able to prove that progressive sharpening
081 occurs generically in high-dimensional models, at least at
082 early times, and we find that the final curvature deviates by
083 a predictable amount from the convergence threshold.

084 **2. Quadratic regression model**

085 We begin by defining our basic *quadratic regression*
086 *model*. Given a P -dimensional parameter vector θ , the
087 D -dimensional output $\mathbf{f}(\theta)$ is given by

$$088 \quad \mathbf{f}(\theta) = \mathbf{y} + \mathbf{G}^\top \theta + \frac{1}{2} \mathbf{Q}(\theta, \theta). \quad (1)$$

089 Here \mathbf{y} is a D -dimensional vector, \mathbf{G} is a $D \times P$ -dimensional
090 matrix, and \mathbf{Q} is a $D \times P \times P$ -dimensional tensor sym-
091 metric in the last two indices - that is, $\mathbf{Q}(\cdot, \cdot)$ takes two P -
092 dimensional vectors as input, and outputs a D -dimensional
093 vector verifying $\mathbf{Q}(\theta, \theta)_\alpha = \theta^\top \mathbf{Q}_\alpha \theta$. If $\mathbf{Q} = \mathbf{0}$, the model
094 corresponds to linear regression. We can recover the $D \times P$ -
095 dimensional Jacobian $\mathbf{J} = \partial \mathbf{f} / \partial \theta$ using

$$096 \quad \mathbf{G}_{\alpha i} = \left. \frac{\partial \mathbf{f}_\alpha}{\partial \theta_i} \right|_{\theta=0}, \quad \mathbf{Q}_{\alpha i j} = \left. \frac{\partial^2 \mathbf{f}_\alpha}{\partial \theta_i \partial \theta_j} \right|_{\theta=0} \rightarrow \mathbf{J} = \mathbf{G} + \mathbf{Q}(\theta, \cdot). \quad (2)$$

097 Any model can be converted into a quadratic regression
098 model by a second-order Taylor expansion around any dif-
099 ferentiable point. Quadratic expansions of shallow MLPs
100 have been previously studied (**Bai & Lee, 2020; Zhu et al.,**
101 **2022a**), and the perturbation theory for small \mathbf{Q} is studied

102 in **Roberts et al. (2022)**. Other related models are detailed
103 in Appendix A. We will provide evidence that even random,
104 unstructured quadratic regression models lead to *edge of*
105 *stability* (EOS) behavior.

106 In this work we focus on the MSE loss setting. More explicitly,
107 given a D -dimensional target vector $\hat{\mathbf{y}}$, the loss $\mathcal{L}(\theta)$
108 can be written in terms of the residuals $\mathbf{z} = \mathbf{f}(\theta) - \hat{\mathbf{y}}$:

$$109 \quad \mathcal{L}(\theta) = \frac{1}{2} \sum_\alpha \mathbf{z}_\alpha^2 = \frac{1}{2} \sum_\alpha \left[\mathbf{y} - \hat{\mathbf{y}} + \mathbf{G}^\top \theta + \frac{1}{2} \mathbf{Q}(\theta, \theta) \right]_\alpha^2. \quad (3)$$

110 As we will show, in this setting the dynamics can be written
111 in function space in terms of \mathbf{z} and \mathbf{J} alone.

3. Low-dimensional dynamics

112 We begin by focusing on the dynamics for $D = 1$ - a single
113 datapoint. Without loss of generality, we can write the loss
114 function as:

$$115 \quad \mathcal{L}(\theta) = \frac{1}{2} \left[\frac{1}{2} [\theta^\top \mathbf{Q} \theta - E] \right]^2 \quad (4)$$

116 for a $P \times P$ matrix \mathbf{Q} and scalar \tilde{E} which define the prob-
117 lem. We will analyze the dynamics in terms of the (scalar)
118 residual $z = \frac{1}{2} [\theta^\top \mathbf{Q} \theta - E]$ and the $1 \times P$ dimensional
119 Jacobian $\mathbf{J} = \partial z / \partial \theta$. In particular, we will be interested
120 in the dynamics of the scalar curvature $\mathbf{J} \mathbf{J}^\top$ (the neural
121 tangent kernel, or NTK).

3.1. Gradient flow

122 We first consider gradient flow (GF) dynamics of the loss \mathcal{L}
123 with respect to the parameters θ . Given a scaling factor η ,
124 the GF dynamics are given by

$$125 \quad \dot{\theta} = -\eta \nabla_\theta \mathcal{L} = -\eta z \frac{\partial z}{\partial \theta} = -\frac{\eta}{2} [\theta^\top \mathbf{Q} \theta - E] \mathbf{Q} \theta. \quad (5)$$

126 The dynamics of z and \mathbf{J} close:

$$127 \quad \dot{z} = -\eta (\mathbf{J} \mathbf{J}^\top) z, \quad \dot{\mathbf{J}} = -\eta z \mathbf{J} \mathbf{Q}. \quad (6)$$

128 The curvature is a scalar, described by the NTK $\mathbf{J} \mathbf{J}^\top$. In
129 these coordinates, we have $E = \mathbf{J} \mathbf{Q}^+ \mathbf{J}^\top - 2z$, where \mathbf{Q}^+
130 denotes the Moore-Penrose pseudoinverse.

131 We can make some coordinate transformations to simplify
132 the dynamics. We define:

$$133 \quad \tilde{z} = \eta z, \quad T(k) = \eta \mathbf{J} \mathbf{Q}^k \mathbf{J}^\top. \quad (7)$$

134 We note that $T(0) = \eta \mathbf{J} \mathbf{J}^\top$ - that is, the curvature normal-
135 ized by the scaling factor. The dynamical equations are:

$$136 \quad \frac{d\tilde{z}}{dt} = -\tilde{z} T(0), \quad \frac{dT(k)}{dt} = -2\tilde{z} T(k+1). \quad (8)$$

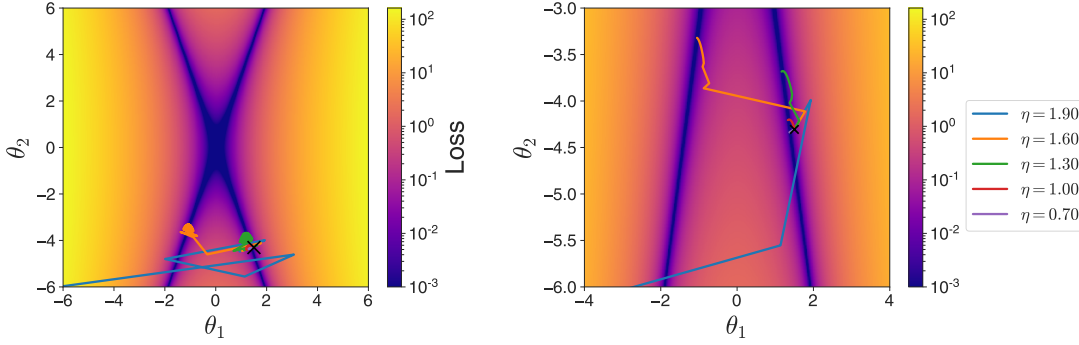


Figure 1. $D = 1$ loss landscape $\mathcal{L}(\cdot)$ as a function of the parameters θ , where $P = 2$, $E = 0$ and \mathbf{Q} has eigenvalues 1 and -0.1 . The GD trajectories (initialized at $(1.5, -4.32)$, marked with an x) converge to minima with larger curvature than at initialization and therefore show progressive sharpening (left). The two-step dynamics, in which we consider only even iteration numbers, exhibit fewer oscillations near the edge of stability (right).

In order to study edge of stability behavior, we need initializations which allow the curvature $T(0)$ to increase over time - a phenomenon known as *progressive sharpening*. Progressive sharpening has been shown to be ubiquitous in machine learning models (Cohen et al., 2022a), so any useful phenomenological model should show it as well. In Appendix B.1, we confirm that the model shows progressive sharpening over a range of initial conditions.

3.2. Gradient descent

We will now show that for gradient descent (GD) dynamics with learning rate η , there is a family of initializations where the $D = 1$ quadratic regression model shows *edge of stability* (EOS) behavior. For this model, we define EOS behavior as a setting where the dynamics causes λ_{\max} , the maximum eigenvalue value of the NTK $\mathbf{J}\mathbf{J}^\top$, to remain close to the critical value $2/\eta$. This critical value corresponds to the largest learning rate where the dynamics converges exponentially near a minimum of the loss \mathcal{L} . This boundary corresponds to $T(0) = 2$ - hence the interpretation of $T(0)$ as the rescaled curvature.

We will show that there is a family of models such that, for any distance, there is a model which leads to EOS convergence to that distance away from the edge of stability - for any initialization in a non-trivial volume of initializations. Additionally we will show that this initialization volume is uniform across models in a natural set of coordinates.

We will prove this form of EOS in $D = 1$ model, and find empirical evidence that this holds for for large D as well. Note that we define the EOS with respect to the maximum NTK eigenvalue instead of the maximum loss Hessian eigenvalue from (Cohen et al., 2022a); see Appendix A.1 for discussion of why this is appropriate for MSE loss.

When \mathbf{Q} has both positive and negative eigenvalues, the loss

landscape is the square of a hyperbolic paraboloid (Figure 1, left). As suggested by the gradient flow analysis, this causes some trajectories to increase their curvature before convergence. The final curvature naturally depends on both the initialization and learning rate. One of the challenges in analyzing the gradient descent dynamics is that they rapidly and heavily oscillate around minima for large learning rates. One way to mitigate this issue is to consider only every other step (Figure 1, right). We will use this observation to analyze the gradient descent (GD) dynamics directly to find configurations where these trajectories show edge-of-stability behavior.

Let θ_t be the parameters at step t . The gradient descent equations are given by:

$$\theta_{t+1} - \theta_t = -\eta \nabla_{\theta} \mathcal{L} = \frac{\eta}{2} [\theta_t^\top \mathbf{Q} \theta_t - E] \mathbf{Q} \theta_t. \quad (9)$$

In the $\tilde{z} - T$ coordinates, the gradient descent equations become (Appendix B.2):

$$\tilde{z}_{t+1} - \tilde{z}_t = -\tilde{z}_t T_t(0) + \frac{1}{2} (\tilde{z}_t^2) T_t(1) \quad (10)$$

$$T_{t+1}(k) - T_t(k) = -\tilde{z}_t (2T_t(k+1) - \tilde{z}_t T_t(k+2)). \quad (11)$$

If \mathbf{Q} is invertible, $\tilde{E} \equiv \eta E = T(-1) - 2\tilde{z}$. By definition $T_t(0) = \eta \mathbf{J}_t \mathbf{J}_t^\top = \eta \lambda_{\max,t}$ is the (rescaled) NTK eigenvalue. In these coordinates, EOS behavior corresponds to dynamics which keep $T_t(0)$ near the value 2 as \tilde{z}_t goes to 0.

In the remainder of this section, we will focus on the $P = 2$ case. As we will see, this lets us write the dynamics in terms of \tilde{z} and $T(0)$ (the residuals and curvature) alone.

3.2.1. REDUCTION TO CATAPULT DYNAMICS

If the eigenvalues of \mathbf{Q} are $\{-\omega, \omega\}$, and $\tilde{E} = 0$, the model becomes equivalent to a single hidden layer linear network

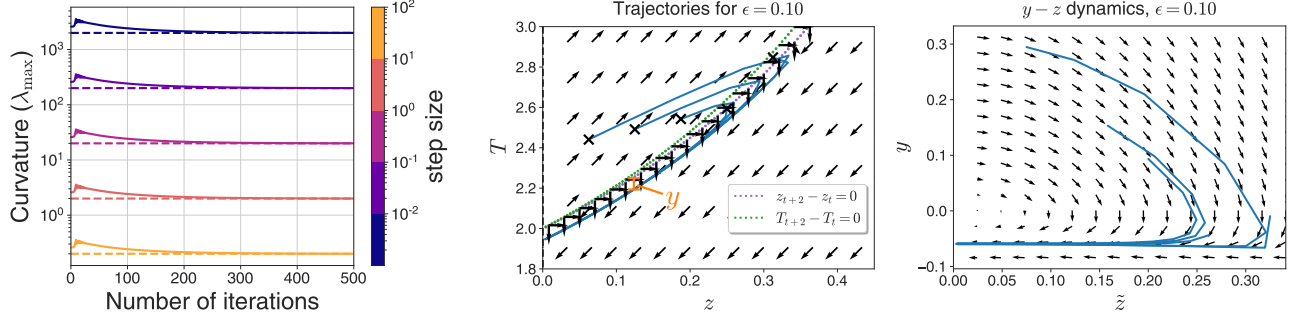


Figure 2. Left: plotting curvature for $D = 1, P = 2$ model shows EOS behavior for various step sizes ($\epsilon = 5 \cdot 10^{-3}$). Middle: plotting every other iterate, we see that a variety of initializations (black x's), trajectories in $\tilde{z} - T(0)$ space stay near the nullcline $(\tilde{z}, f_{\tilde{z}}(\tilde{z}))$ - the curve where $\tilde{z}_{t+2} - \tilde{z}_t = 0$. Arrows represent direction of dynamical flows. Right: Changing variables to $y = T(0) - f_{\tilde{z}}(\tilde{z})$ shows quick concentration to a curve of near-constant, small, negative y .

with one training datapoint (Appendix A.2) - also known as the catapult phase dynamics. This model doesn't exhibit sharpening or edge-of-stability behavior (Lewkowycz et al., 2020). We can prove this in the $\tilde{z} - T(0)$ coordinates.

We assume without loss of generality that the eigenvalues are $\{-1, 1\}$ - which can be accomplished by rescaling \tilde{z} . We can rewrite the dynamics in terms of \tilde{z} and the curvature $T(0)$ only (Appendix B.3):

$$\tilde{z}_{t+1} - \tilde{z}_t = -\tilde{z}_t T_t(0) + \frac{1}{2}(\tilde{z}_t^2)(2\tilde{z}_t + \tilde{E}) \quad (12)$$

$$T_{t+1}(0) - T_t(0) = -2\tilde{z}_t(2\tilde{z}_t + \tilde{E}) + \tilde{z}_t^2 T_t(0). \quad (13)$$

For $\tilde{E} = 0$, we can see that $\text{sign}(\Delta T(0)) = \text{sign}(T_t(0) - 4)$, as in (Lewkowycz et al., 2020) - so convergence implies strictly decreasing curvature. For $\tilde{E} \neq 0$, there is a region where the curvature can increase (Appendix B.3). However, there is still no EOS behavior - if $\mathbf{J}\mathbf{J}^\top$ starts away from $2/\eta$, there is no mechanism to stabilize it near the edge.

3.2.2. EDGE OF STABILITY REGIME

In this section, we consider the case in which \mathbf{Q} has two eigenvalues - one of which is large and positive, and the other one small and negative. Without loss of generality, we assume that the largest eigenvalue of \mathbf{Q} is 1. We denote the second eigenvalue by $-\epsilon$, for $0 < \epsilon \leq 1$. With this notation we can write the dynamical equations (Appendix B.3) as

$$\tilde{z}_{t+1} - \tilde{z}_t = -\tilde{z}_t T_t(0) + \frac{1}{2}(\tilde{z}_t^2)((1-\epsilon)T_t(0) + \epsilon(2\tilde{z}_t + \tilde{E})) \quad (14)$$

$$\begin{aligned} T_{t+1}(0) - T_t(0) = & -2\tilde{z}_t(\epsilon(2\tilde{z}_t + \tilde{E}) + (1-\epsilon)T_t(0)) \\ & + \tilde{z}_t^2 [T_t(0) + \epsilon(\epsilon-1)(T_t(0) - \tilde{E} - 2\tilde{z}_t)]. \end{aligned} \quad (15)$$

For small ϵ , there are trajectories where λ_{\max} is initially away from $2/\eta$ but converges towards it (Figure 2, left) - in other words, EOS behavior. We used a variety of step sizes η but initialized at pairs initialized at pairs $(\eta z_0, \eta T_0(0))$ to show the universality of the $\tilde{z}-T(0)$ coordinates.

In order to quantitatively understand the progressive sharpening and edge of stability, it is useful to look at the two-step dynamics. One additional motivation for studying the two-step dynamics follows from the analysis of gradient descent on linear least squares (i.e., linear model) with a large step size λ . For every coordinate $\tilde{\theta}$, the one-step and two-step dynamics are

$$\tilde{\theta}_{t+1} - \tilde{\theta}_t = -\lambda \tilde{\theta}_t \text{ and } \tilde{\theta}_{t+2} - \tilde{\theta}_t = (1-\lambda)^2 \tilde{\theta}_t \quad (16)$$

While the dynamics converge for $\lambda < 2$, if $\lambda > 1$ the one-step dynamics alternate sign when approaching minimum, whereas the the two-step dynamics maintain the sign of $\tilde{\theta}$ and the trajectories exhibit no oscillations.

Likewise, plotting every other iterate in the two parameter model more clearly demonstrates the phenomenology. For small ϵ , the dynamics shows the distinct phases described in (Li et al., 2022): an initial increase in $T(0)$, a slow increase in \tilde{z} , then a decrease in $T(0)$, and finally a slow decrease of \tilde{z} while $T(0)$ remains near 2 (Figure 2, middle).

Unfortunately, the two-step version of the dynamics defined by Equations 14 and 15 are more complicated - they are 3rd order in $T(0)$ and 9th order in \tilde{z} ; see Appendix B.4 for a more detailed discussion. However, we can analyze the dynamics as \tilde{z} goes to 0. In order to understand the mechanisms of the EOS behavior, it is useful to understand the *nullclines* of the two step dynamics. The nullclines are the curves $(\tilde{z}, f_{\tilde{z}}(\tilde{z}))$ and $(\tilde{z}, f_T(\tilde{z}))$ consisting of initializations such that \tilde{z} and $T(0)$, respectively, are unchanged after two steps.

We define the multinomials $p_{\tilde{z}}(\tilde{z}, T)$ and $p_T(\tilde{z}, T)$ such that

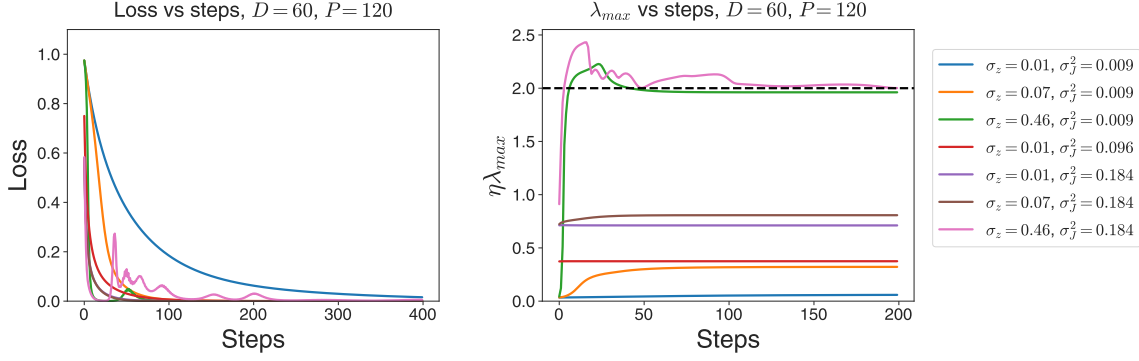


Figure 3. GD dynamics in the quadratic regression model. Loss functions are monotonic for small σ_z (left). For larger σ_z , final λ_{max} is higher (right). As sharpening drives $\eta\lambda_{max}$ near 2, non-linear effects induce EOS behavior.

$\tilde{z}_{t+1} - \tilde{z}_t = p_{\tilde{z}}(\tilde{z}_t, T_t)$ and $T_{t+1}(0) - T_t(0) = p_T(\tilde{z}_t, T_t)$.

Then $f_{\tilde{z}}(\tilde{z})$ and $f_T(\tilde{z})$ obey the implicit equations:

$$\begin{aligned} p_{\tilde{z}}(p_{\tilde{z}}(\tilde{z}, f_{\tilde{z}}(\tilde{z})), p_T(\tilde{z}, f_{\tilde{z}}(\tilde{z}))) &= 0, \\ p_T(p_{\tilde{z}}(\tilde{z}, f_T(\tilde{z})), p_T(\tilde{z}, f_T(\tilde{z}))) &= 0 \end{aligned} \quad (17)$$

These expressions are polynomials cubic in $f_{\tilde{z}}(\tilde{z})$ and $f_T(\tilde{z})$ respectively - so there are three possible solutions as \tilde{z} goes to 0. We are particularly interested in the solution that goes through $\tilde{z} = 0, T(0) = 2$ - that is, the critical point corresponding to EOS.

Calculations detailed in Appendix B.4 show that the distance between the two nullclines is linear in ϵ , so they become close as ϵ goes to 0. (Figure 2, middle). In addition, the trajectories stay near $f_{\tilde{z}}$ - which gives rise to EOS behavior. This suggests that the dynamics are slow near the nullclines, and trajectories appear to be approaching an attractor. We can find the structure of the attractor by changing variables to $y_t \equiv T_t(0) - f_{\tilde{z}}(\tilde{z}_t)$ - the distance from the \tilde{z} nullcline.

We can build intuition by expanding the dynamics to lowest order in \tilde{z} and y . A direct calculation in Appendix B.5 gives us the approximation:

$$\tilde{z}_{t+2} - \tilde{z}_t = 2y_t\tilde{z}_t + O(y_t^2\tilde{z}_t) + O(y_t\tilde{z}_t^2) \quad (18)$$

$$y_{t+2} - y_t = -2(4 - 3\epsilon + 4\epsilon^2)y_t\tilde{z}_t^2 - 4\epsilon\tilde{z}_t^2 + O(\epsilon\tilde{z}_t^3 + y_t^2\tilde{z}_t^2) \quad (19)$$

We immediately see that \tilde{z} changes slowly for small y - since we chose coordinates where $\tilde{z}_{t+2} - \tilde{z}_t = 0$ when $y = 0$. We can also see that $y_{t+2} - y_t$ is $O(\epsilon)$ for $y_t = 0$ - so for small ϵ , the y dynamics is slow too. Moreover, we see that the coefficient of the $\epsilon\tilde{z}_t^2$ term is negative - the changes in \tilde{z} tend to drive y (and therefore $T(0)$) to decrease. The coefficient of the y_t term is negative as well; the dynamics of y tends to be contractive. The key is that the contractive behavior takes y to an $O(\epsilon)$ fixed point at a rate proportional to \tilde{z}^2 , while the dynamics of \tilde{z} are proportional to ϵ . This suggests a separation of timescales if $\tilde{z}^2 \gg \epsilon$, where y first equilibrates to a fixed value, and then \tilde{z} converges to 0 (Figure 2, right).

The intuition from the lowest order terms can be formalized, and gives us a prediction of $\lim_{t \rightarrow \infty} y_t = -\epsilon/2$, confirmed by the following theorem (proof in Appendix B.6):

Theorem 3.1. Consider a quadratic regression model with $D = 1, P = 2, \tilde{E} = 0$, and \mathbf{Q} with eigenvalues $\{-\epsilon, 1\}$. There exists an $\epsilon_c > 0$ and an ϵ -independent neighborhood $U \in \mathbb{R}^3$ such that for $0 < \epsilon < \epsilon_c$ and all initializations such that $(\tilde{z}_0, \eta\lambda_{max}(0), \eta) \in U$, sharpness converges to a value near the edge of stability:

$$\lim_{t \rightarrow \infty} \lambda_{max}(t) = (2 - \epsilon/2)/\eta + O(\epsilon^2). \quad (20)$$

Therefore, unlike the catapult phase model, the small ϵ provably has EOS behavior - whose mechanism is well-understood by the $\tilde{z} - y$ coordinate transformation.

4. High dimensional dynamics

In this section we analyze the dynamics for large D . We focus on randomly initialized \mathbf{Q} , and prove that progressive sharpening is ubiquitous. We then demonstrate that the quadratic regression model shows edge of stability behavior over a range of initializations.

4.1. Gradient flow dynamics

The gradient flow dynamics on an MSE loss function \mathcal{L} can be written generally as

$$\dot{\theta} = -\frac{\partial \mathcal{L}(\mathbf{z})}{\partial \theta} = -\mathbf{J}^\top \mathbf{z}. \quad (21)$$

where \mathbf{J} is the $D \times P$ -dimensional Jacobian, and \mathbf{z} is the D -dimensional vector of residuals $\mathbf{f}(\theta) - \hat{\mathbf{y}}$. For the quadratic regression model, the dynamics in \mathbf{z} and \mathbf{J} once again close:

$$\dot{\mathbf{z}} = \mathbf{J}\dot{\theta} = -\mathbf{J}\mathbf{J}^\top \mathbf{z}, \quad \dot{\mathbf{J}} = -\mathbf{Q}(\mathbf{J}^\top \mathbf{z}, \cdot). \quad (22)$$

When $\mathbf{Q} = \mathbf{0}$ (linearized regime), \mathbf{J} is constant, the dynamics are then linear in \mathbf{z} , and are controlled by the eigenstructure of the $D \times D$ matrix $\mathbf{J}\mathbf{J}^\top$, the empirical NTK.

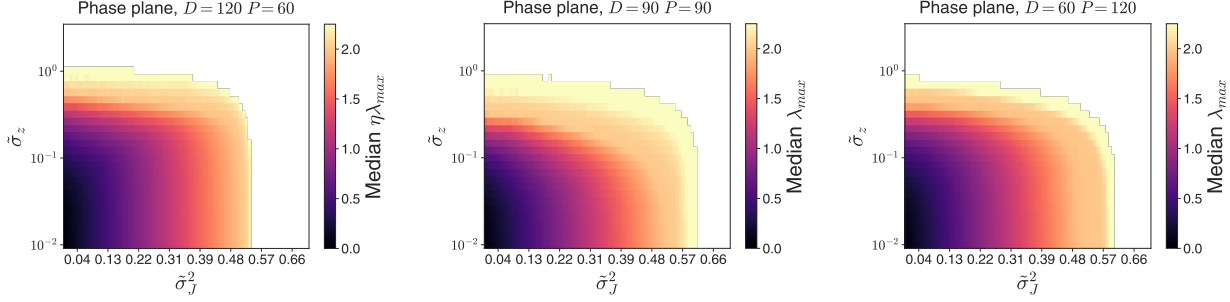


Figure 4. $\tilde{\sigma}_z/\tilde{\sigma}_J^2$ phase planes for quadratic regression models, for various D and P . Models were initialized with 100 random seeds for each $\tilde{\sigma}_z$, $\tilde{\sigma}_J$ pair and iterated until convergence. For each pair $\tilde{\sigma}_z$, $\tilde{\sigma}_J^2$ we plot the median λ_{\max} of the NTK $\mathbf{J}^\top \mathbf{J}$. For intermediate $\tilde{\sigma}_z$, where both sharpening and non-linear \mathbf{z} dynamics occur, trajectories tend to converge so λ_{\max} of the NTK is near $2/\eta$ (EOS).

We are interested in settings where progressive sharpening occurs under GF. We can study the dynamics of the maximum eigenvalue λ_{\max} of $\mathbf{J}\mathbf{J}^\top$ at early times for random initializations. In Appendix C.1, we prove the following theorem:

Theorem 4.1. *Let \mathbf{z} , \mathbf{J} , and \mathbf{Q} be initialized with i.i.d. elements with zero mean and variances σ_z^2 , σ_J^2 , and 1 respectively, with distributions invariant to rotation in data and parameter space, and have finite fourth moments. Let λ_{\max} be the largest eigenvalue of $\mathbf{J}\mathbf{J}^\top$. In the limit of large D and P , with fixed ratio D/P , at initialization we have*

$$\mathbb{E}[\dot{\lambda}_{\max}(0)] = 0, \quad \mathbb{E}[\ddot{\lambda}_{\max}(0)]/\mathbb{E}[\lambda_{\max}(0)] = \sigma_z^2 \quad (23)$$

where \mathbb{E} denotes the expectation over \mathbf{z} , \mathbf{J} , and \mathbf{Q} at initialization.

Much like in the $D = 1$ case, Theorem 4.1 suggests that it is easy to find initializations that show progressive sharpening - and increasing σ_z makes sharpening more prominent.

4.2. Gradient descent dynamics

We now consider finite-step size gradient descent (GD) dynamics. The dynamics for θ are given by:

$$\theta_{t+1} = \theta_t - \eta \mathbf{J}_t^\top \mathbf{z}_t. \quad (24)$$

In this setting, the dynamical equations can be written as

$$\mathbf{z}_{t+1} - \mathbf{z}_t = -\eta \mathbf{J}_t \mathbf{J}_t^\top \mathbf{z}_t + \frac{1}{2} \eta^2 \mathbf{Q}(\mathbf{J}_t^\top \mathbf{z}_t, \mathbf{J}_t^\top \mathbf{z}_t) \quad (25)$$

$$\mathbf{J}_{t+1} - \mathbf{J}_t = -\eta \mathbf{Q}(\mathbf{J}_t^\top \mathbf{z}_t, \cdot). \quad (26)$$

If $\mathbf{Q} = \mathbf{0}$, the dynamics reduce to discrete gradient descent in a quadratic potential - which converges iff $\lambda_{\max} < 2/\eta$.

One immediate question is: when does the η^2 in Equation 25 affect the dynamics? Given that it scales with higher powers of η and \mathbf{z} than the first term, we can conjecture that the

ratio of the magnitudes of the terms, r_{NL} , is proportional to $\|\mathbf{z}\|_2$ and η . A calculation in Appendix C.2 shows that, for random rotationally invariant initializations, we have:

$$r_{NL} \equiv \left(\frac{\mathbb{E}[\|\frac{1}{2}\eta^2 \mathbf{Q}(\mathbf{J}_0^\top \mathbf{z}_0, \mathbf{J}_0^\top \mathbf{z}_0)\|_2^2]}{\mathbb{E}[\|\eta \mathbf{J}_0 \mathbf{J}_0^\top \mathbf{z}_0\|_2^2]} \right)^{1/2} = \frac{1}{2} \eta \sigma_z D, \quad (27)$$

where the initialization statistics are defined as in Theorem 4.1. This confirms that increasing the learning rate and the residual magnitude $\|\mathbf{z}\|$ increases the deviation of the dynamics from GF, and reveals that the amount of non-linearity is insensitive to \mathbf{J} .

We can see this phenomenology in the dynamics of the GD equations (Figure 3). Here we plot different trajectories for random initializations of the type in Theorem 4.1 with $D = 60$, $P = 120$, and $\eta = 1$. As σ_z increases, so does the curvature λ_{\max} (as suggested by Theorem 4.1), and when σ_z is $O(1)$, the dynamics is non-linear (as predicted by r_{NL}) and EOS behavior emerges. This suggests that the second term in Equation 25 is crucial for the stabilization of λ_{\max} .

We can confirm this more generally by initializing over various η , D , P , σ_z , and σ_J over multiple seeds, and plotting the resulting phase diagram of the final λ_{\max} reached. We can simplify the plotting with some rescaling of parameters and initializations. In the rescaled variables

$$\tilde{\mathbf{z}} = \eta \mathbf{z}, \quad \tilde{\mathbf{J}} = \eta^{1/2} \mathbf{J}, \quad (28)$$

the dynamics are equivalent to Equations 25 and 26 with $\eta = 1$. As in the $\tilde{\mathbf{z}} - T(0)$ model of Equations 56–57, λ_{\max} in the rescaled coordinates is equivalent to $\eta \lambda_{\max}$ in the unscaled coordinates. We can also define rescaled initializations for \mathbf{z} and \mathbf{J} . If we set

$$\sigma_z = \tilde{\sigma}_z/D, \quad \sigma_J = \tilde{\sigma}_J / (DP)^{1/4}, \quad (29)$$

then we have $r_{NL} = \tilde{\sigma}_z$ which allows for easier comparison across (D, P) pairs.

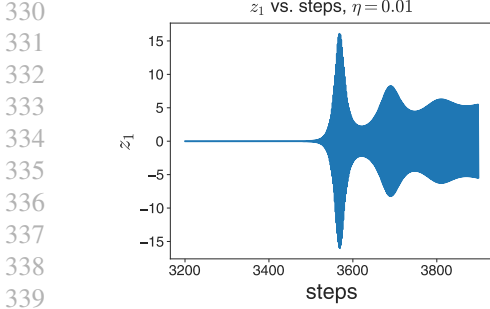


Figure 5. A FCN trained on CIFAR shows multiple cycles of sharpening and edge-of-stability behavior. z_1 , the projection of the training set residuals $f(\mathbf{X}, \boldsymbol{\theta}) - \mathbf{Y}$ onto the top NTK eigenmode \mathbf{v}_1 , increases in magnitude and oscillates around 0 (left). Plotting dynamics every two steps removes high frequency oscillations (middle). The largest eigenvalue λ_1 crosses the edge of stability multiple times, but the second largest eigenvalue λ_2 remains below the edge of stability (right). **Dynamics is similar for Hessian eigenvalues (dashed).**

Using this initialization scheme, we can plot the final value of λ_{\max} reached as a function of $\tilde{\sigma}_z$ and $\tilde{\sigma}_J$ for 100 independent random initializations for each $\tilde{\sigma}_z$, $\tilde{\sigma}_J$ pair (Figure 4). We see that the key is for $r_{NL} = \tilde{\sigma}_z$ to be $O(1)$ - corresponding to both progressive sharpening and non-linear dynamics near initialization. In particular, initializations with small $\tilde{\sigma}_J$ values which converge at the EOS correspond to trajectories which first sharpen, and then settle near $\lambda_{\max} = 2/\eta$. Large $\tilde{\sigma}_z$ and large $\tilde{\sigma}_J$ dynamics diverge. There is a small band of initial $\tilde{\sigma}_J$ over a wide range of $\tilde{\sigma}_z$ which have final $\lambda_{\max} \approx 2/\eta$; these correspond to models initialized near the EOS, which stay near it.

This suggests that progressive sharpening and edge of stability aren't uniquely features of neural network models, and could be a more general property of learning in high-dimensional, non-linear models.

5. Connection to real world models

In this section we conduct numerical experiments in “real world” models, and compare the behavior to our theory on simplified models. Following (Cohen et al., 2022a), we trained a 2-hidden layer tanh network using the squared loss on 5000 examples from CIFAR10 with learning rate 10^{-2} - a setting which shows edge of stability behavior. Close to the onset of EOS, we approximately computed λ_1 , the largest eigenvalue of $\mathbf{J}\mathbf{J}^\top$, and its corresponding eigenvector \mathbf{v}_1 using a Lanczos method (Ghorbani et al., 2019; Novak et al., 2019). We use \mathbf{v}_1 to compute $z_1 = \mathbf{v}_1^\top \mathbf{z}$, where \mathbf{z} is the vector of residuals $f(\mathbf{X}, \boldsymbol{\theta}) - \mathbf{Y}$ for neural network function f , training inputs \mathbf{X} , labels \mathbf{Y} , and parameters $\boldsymbol{\theta}$. The EOS behavior in the NTK is similar to the EOS behavior defined with respect to the full Hessian in (Cohen et al., 2022a) (Figure 5, left and right). Once again, plotting the trajectories at every other step gets rid of the high frequency oscillations (Figure 5, middle). Unlike the $D = 1, P = 2$ model, there are multiple crossings of the

critical line $\lambda_{\max} = 2/\eta$ line.

There is evidence that low-dimensional features of a quadratic regression model could be used to explain some aspects of EOS behavior. We empirically compute the the second derivative of the output $f(\mathbf{x}, \boldsymbol{\theta})$ by automatic differentiation. We denote by $\mathbf{Q}(\cdot, \cdot)$ the resulting tensor. We can use matrix-vector products to compute the spectrum of the matrix $\mathbf{Q}_1 \equiv \mathbf{v}_1 \cdot \mathbf{Q}(\cdot, \cdot)$, which is projection of the output of \mathbf{Q} in the \mathbf{v}_1 direction, without instantiating \mathbf{Q} in memory (Figure 6, left). This figure reveals that the spectrum does not shift much from step 3200 to 3900 (the range of our plots). This suggests that \mathbf{Q} doesn't change much as these EOS dynamics are displayed. We can also see that \mathbf{Q} is much larger in the \mathbf{v}_1 direction than a random direction.

Let y be defined as $y = \lambda_1 \eta - 2$. Plotting the two-step dynamics of z_1 versus $2yz$ we see a remarkable agreement (Figure 6, middle). This is the same form that the dynamics of \tilde{z} takes in our simplified model. It can also be found by iterating Equation 25 twice with fixed Jacobian for $y = \lambda_1 \eta - 2$ and discarding terms higher order in η . This suggests that during this particular EOS behavior, much like in our simplified model the dynamics of the eigenvalue is more important than any rotation in the eigenbasis.

The dynamics of y is more complicated; $y_{t+2} - y_t$ is anticorrelated with z_1^2 but there is no low-order functional form in terms of y and z_1 (Appendix D.2). We can get some insight into the stabilization by plotting the ratio of $\eta^2 \mathbf{Q}_1(\mathbf{J}z_1 \mathbf{v}_1, \mathbf{J}z_1 \mathbf{v}_1)$ (the non-linear contribution to the z_1 dynamics from the \mathbf{v}_1 direction) and $\lambda_1 z_1$ (the linearized contribution), and compare it to the dynamics of y (Figure 6, right). The ratio is small during the initial sharpening, but becomes $O(1)$ shortly before the curvature decreases for the first time. It remains $O(1)$ through the rest of the dynamics. This suggests that the non-linear feedback from the dynamics of the top eigenmode onto itself is crucial to understanding the EOS dynamics.

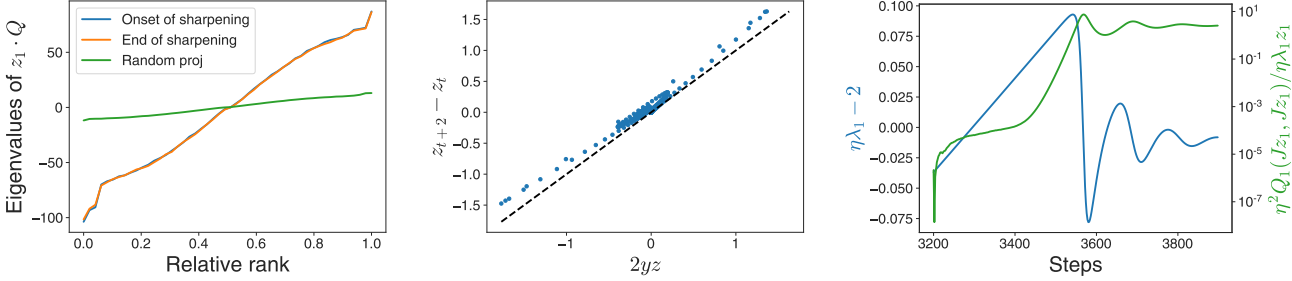


Figure 6. \mathbf{Q} is approximately constant during edge-of-stability dynamics for FCN trained on CIFAR10 (left). Projection onto largest eigendirection \mathbf{v}_1 (blue and orange) is larger than projection onto random direction (green). Two step difference $(z_1)_{t+2} - (z_1)_t$ is well approximated by $2z_1y$ (middle), leading order term of models with fixed eigenbasis. Non-linear dynamical contribution $\eta^2 \mathbf{Q}_1(\mathbf{J} z_1 \mathbf{v}_1, \mathbf{J} z_1 \mathbf{v}_1)$ is small during sharpening, but becomes large immediately preceding decrease in top eigenvalue (right) - as is the case in the simple model.

6. Discussion

6.1. Lessons learned from quadratic regression models

The main lesson to be learned from the quadratic regression models is that behavior like progressive sharpening (for both GF and GD) and edge-of-stability behavior (for GD) may be common features of high-dimensional gradient-based training of non-linear models. Indeed, these phenomena can be revealed in simple settings without any connection to deep learning models: with mild tuning our simplified model, which corresponds to 1 datapoint and 2 parameters can provably show EOS behavior. This combined with the analysis of the CIFAR model suggest that the general mechanism may have a low-dimensional description.

Quadratic approximations of real models quantitatively can capture the early features of EOS behavior (the initial return to $\lambda_{max} < 2/\eta$), but do not necessarily capture the magnitude and period of subsequent oscillations – these require higher order terms (Appendix D.3). Nevertheless, the quadratic approximation does correctly describe much of the qualitative behavior, including the convergence of λ_{max} to a limiting two-cycle that oscillates around $2/\eta$, with an average value *below* $2/\eta$. In the simplified two-parameter model, it is possible to analytically predict the final value at convergence, and indeed we find that it deviates slightly from the value $2/\eta$. **In addition, both the theoretical and realistic models suggest that the curvature is controlled by a low-dimensional feedback mechanism mediated by z_1^2 , mediated via \mathbf{Q}_1 .**

A key feature of all the models studied in this work is that looking at every-other iterate (the two-step dynamics) greatly aids in understanding the models theoretically and empirically. Near the edge of stability, this makes the changes in the top eigenmode small. In the simplified model, the slow \tilde{z} dynamics (and related slow $T(0)$ dynamics) allowed for the detailed theoretical analysis; in

the CIFAR model, the two-step dynamics is slowly varying in both z_1 and λ_{max} . The quantitative comparisons of these small changes may help uncover any universal mechanisms/canonical forms that explain EOS behavior in other systems and scenarios.

6.2. Future work

One avenue for future work is to quantitatively understand progressive sharpening and EOS behavior in the quadratic regression model for large D and P . In particular, computing the final deviation $2 - \eta\lambda_{max}$ in the edge-of-stability regime as a function of σ_z , σ_J , and D/P remains an interesting open question. It would also be useful to understand how higher order terms affect the training dynamics - particularly the details of the oscillations around $y = 2$.

Finally, our analysis has not touched on the feature learning aspects of the model. In the quadratic regression model, feature learning is encoded in the relationship between \mathbf{J} and \mathbf{z} , and in particular the relationship between \mathbf{z} and the eigenstructure of $\mathbf{J}\mathbf{J}^\top$. Understanding how \mathbf{Q} mediates the dynamics of these two quantities may provide a quantitative basis for understanding feature learning which is complementary to existing theoretical approaches (Roberts et al., 2022; Bordelon & Pehlevan, 2022; Yang et al., 2022).

References

- Bai, Y. and Lee, J. D. Beyond Linearization: On Quadratic and Higher-Order Approximation of Wide Neural Networks. In *International Conference on Learning Representations*, March 2020.
- Bordelon, B. and Pehlevan, C. Self-Consistent Dynamical Field Theory of Kernel Evolution in Wide Neural Networks, May 2022.
- Cohen, J., Kaur, S., Li, Y., Kolter, J. Z., and Talwalkar, A.

- 440 Gradient Descent on Neural Networks Typically Occurs
 441 at the Edge of Stability. In *International Conference on*
 442 *Learning Representations*, February 2022a.
- 443 Cohen, J. M., Ghorbani, B., Krishnan, S., Agarwal, N.,
 444 Medapati, S., Badura, M., Suo, D., Cardoze, D., Nado, Z.,
 445 Dahl, G. E., and Gilmer, J. Adaptive Gradient Methods
 446 at the Edge of Stability, July 2022b.
- 447 Damian, A., Nichani, E., and Lee, J. D. Self-Stabilization:
 448 The Implicit Bias of Gradient Descent at the Edge of
 449 Stability, September 2022.
- 450 Foret, P., Kleiner, A., Mobahi, H., and Neyshabur, B.
 451 Sharpness-aware Minimization for Efficiently Improving
 452 Generalization. In *International Conference on Learning*
 453 *Representations*, April 2022.
- 454 Ghorbani, B., Krishnan, S., and Xiao, Y. An Investigation
 455 into Neural Net Optimization via Hessian Eigenvalue
 456 Density. In *Proceedings of the 36th International Conference*
 457 *on Machine Learning*, pp. 2232–2241. PMLR, May
 458 2019.
- 459 Giladi, N., Nacson, M. S., Hoffer, E., and Soudry, D. At
 460 Stability’s Edge: How to Adjust Hyperparameters to Pre-
 461 serve Minima Selection in Asynchronous Training of
 462 Neural Networks? In *Eighth International Conference*
 463 *on Learning Representations*, April 2020.
- 464 Gilmer, J., Ghorbani, B., Garg, A., Kudugunta, S.,
 465 Neyshabur, B., Cardoze, D., Dahl, G. E., Nado, Z., and
 466 Firat, O. A Loss Curvature Perspective on Training In-
 467 stabilities of Deep Learning Models. In *International*
 468 *Conference on Learning Representations*, March 2022.
- 469 Huang, J. and Yau, H.-T. Dynamics of Deep Neural Net-
 470 works and Neural Tangent Hierarchy. In *Proceedings of*
 471 *the 37th International Conference on Machine Learning*,
 472 pp. 4542–4551. PMLR, November 2020.
- 473 Jacot, A., Gabriel, F., and Hongler, C. Neural Tangent Ker-
 474 nel: Convergence and Generalization in Neural Networks.
 475 In *Advances in Neural Information Processing Systems*
 476 *31*, pp. 8571–8580. Curran Associates, Inc., 2018.
- 477 Lee, J., Xiao, L., Schoenholz, S., Bahri, Y., Novak, R., Sohl-
 478 Dickstein, J., and Pennington, J. Wide Neural Networks
 479 of Any Depth Evolve as Linear Models Under Gradient
 480 Descent. In *Advances in Neural Information Process-
 481 ing Systems 32*, pp. 8570–8581. Curran Associates, Inc.,
 482 2019.
- 483 Lewkowycz, A., Bahri, Y., Dyer, E., Sohl-Dickstein, J.,
 484 and Gur-Ari, G. The large learning rate phase of deep
 485 learning: The catapult mechanism. March 2020.
- 486 Li, Z., Wang, Z., and Li, J. Analyzing Sharpness along GD
 487 Trajectory: Progressive Sharpening and Edge of Stability,
 488 July 2022.
- 489 Neyshabur, B., Bhojanapalli, S., Mcallester, D., and Srebro,
 490 N. Exploring Generalization in Deep Learning. In *Ad-
 491 vances in Neural Information Processing Systems 30*, pp.
 492 5947–5956. Curran Associates, Inc., 2017.
- 493 Novak, R., Xiao, L., Hron, J., Lee, J., Alemi, A. A.,
 494 Sohl-Dickstein, J., and Schoenholz, S. S. Neural Tan-
 495 gents: Fast and Easy Infinite Neural Networks in Python.
 496 *arXiv:1912.02803 [cs, stat]*, December 2019.
- 497 Roberts, D. A., Yaida, S., and Hanin, B. *The Principles*
 498 *of Deep Learning Theory*. May 2022. doi: 10.1017/
 499 9781009023405.
- 500 Wu, L., Ma, C., and E, W. How SGD Selects the Global
 501 Minima in Over-parameterized Learning: A Dynamical
 502 Stability Perspective. In *Advances in Neural Information*
 503 *Processing Systems*, volume 31. Curran Associates, Inc.,
 504 2018.
- 505 Yang, G. Tensor Programs I: Wide Feedforward or Recur-
 506 rent Neural Networks of Any Architecture are Gaussian
 507 Processes. *arXiv:1910.12478 [cond-mat, physics:math-
 508 ph]*, May 2021.
- 509 Yang, G., Hu, E. J., Babuschkin, I., Sidor, S., Liu, X., Farhi,
 510 D., Ryder, N., Pachocki, J., Chen, W., and Gao, J. Tensor
 511 Programs V: Tuning Large Neural Networks via Zero-
 512 Shot Hyperparameter Transfer, March 2022.
- 513 Zhu, L., Liu, C., Radhakrishnan, A., and Belkin, M.
 514 Quadratic models for understanding neural network dy-
 515 namics, May 2022a.
- 516 Zhu, X., Wang, Z., Wang, X., Zhou, M., and Ge, R. Un-
 517 derstanding Edge-of-Stability Training Dynamics with a
 518 Minimalist Example, October 2022b.

A. Connection to other models

A.1. Hessian versus NTK maximum eigenvalue

In this work we focus on EOS dynamics of the largest eigenvalue of the NTK, rather than the Hessian as in (Cohen et al., 2022a). We note that a version of Theorem 3.1 is true for the maximum Hessian eigenvalue as well. In general, the Hessian can be written as

$$\frac{\partial^2 \mathcal{L}}{\partial \theta \partial \theta'} = \nabla \mathcal{L} \cdot \frac{\partial^2 \mathbf{z}}{\partial \theta \partial \theta'} + \mathbf{J}^T \frac{\partial^2 \mathcal{L}}{\partial \mathbf{z} \partial \mathbf{z}'} \mathbf{J} \quad (30)$$

For squared loss in particular, we have

$$\frac{\partial^2 \mathcal{L}}{\partial \theta \partial \theta'} = \nabla \mathcal{L} \cdot \frac{\partial^2 \mathbf{z}}{\partial \theta \partial \theta'} + \mathbf{J}^T \mathbf{J} \quad (31)$$

As the loss gradient goes to 0, the Hessian eigenvalues approach the eigenvalues of $\mathbf{J}\mathbf{J}^T$ - whose non-zero eigenvalues are the same as those of the empirical NTK $\mathbf{J}\mathbf{J}^T$. Since the theorem involves behavior as \tilde{z} goes to convergence, the maximum NTK and maximum Hessian eigenvalues are equal in the limit, and the same EOS behavior applied in both cases.

For the higher dimensional models (quadratic regression model and fully connected network on CIFAR10), our experiments show that the maximum NTK eigenvalue shows edge of stability behavior. The CIFAR model is the same as the one in (Cohen et al., 2022a) which was used to illustrate the edge of stability in terms of the maximum Hessian eigenvalues. Therefore we focused on the NTK version of EOS in our paper, as we found it more amenable to theoretical analysis and explanation.

There are almost certainly cases where EOS behavior is displayed in the Hessian eigenvalues but not the NTK eigenvalues, particularly in cases where the loss is highly non-isotropic in the outputs (that is, $\frac{\partial^2 \mathcal{L}}{\partial \mathbf{z} \partial \mathbf{z}'}$ is far from a multiple of the identity matrix). As pointed out in previous works in these cases even the Hessian-based EOS is more difficult to analyze (Cohen et al., 2022a). We leave understanding of EOS with more complicated loss functions for future work.

A.2. One-hidden layer linear network

Consider a one hidden layer network with a scalar output:

$$f(\mathbf{x}) = \mathbf{v}^\top \mathbf{U} \mathbf{x} \quad (32)$$

where \mathbf{x} is an input vector of length N , \mathbf{U} is a $K \times N$ dimensional matrix, and \mathbf{v} is a K dimensional vector. We note that

$$\frac{\partial^2 f(\mathbf{x})}{\partial \mathbf{v}_i \partial \mathbf{v}_j} = \frac{\partial^2 f(\mathbf{x})}{\partial \mathbf{U}_{ij} \partial \mathbf{U}_{kl}} = 0, \quad \frac{\partial^2 f(\mathbf{x})}{\partial \mathbf{v}_i \partial \mathbf{U}_{jk}} = \delta_{ij} \mathbf{x}_k \quad (33)$$

where δ_{ij} is the Kroenecker delta. For a fixed training set, this second derivative is constant; therefore, the one-hidden layer linear network is a quadratic regression model of the type studied in Section 4.

In the particular case of a single datapoint \mathbf{x} , we can compute the eigenvectors of the \mathbf{Q} matrix. Let (\mathbf{w}, \mathbf{W}) be an eigenvector of \mathbf{Q} , representing the \mathbf{v} and \mathbf{U} components respectively. The eigenvector equations are

$$\omega \mathbf{w}_i = \mathbf{x}_m \delta_{ij} \mathbf{W}_{jm} \quad (34)$$

$$\omega \mathbf{W}_{jm} = \mathbf{x}_m \delta_{ij} \mathbf{w}_i \quad (35)$$

Simplifying, we have:

$$\omega \mathbf{w} = \mathbf{W} \mathbf{x} \quad (36)$$

$$\omega \mathbf{W} = \mathbf{w} \mathbf{x}^\top \quad (37)$$

We have two scenarios. The first is that $\omega = 0$. In this case, we have $\mathbf{w} = 0$, and \mathbf{W} is a matrix with \mathbf{x} in its nullspace. The latter condition gives us M constraints on $M \times N$ equations - for a total of $M(N - 1)$ of our $M(N + 1)$ total eigenmodes.

If $\omega \neq 0$, then combining the equations we have the conditions:

$$\omega^2 \mathbf{w} = (\mathbf{x} \cdot \mathbf{x}) \mathbf{w} \quad (38)$$

$$\omega^2 \mathbf{W} = \mathbf{W} \mathbf{x} \mathbf{x}^\top \quad (39)$$

This gives us $\omega = \pm\sqrt{\mathbf{x} \cdot \mathbf{x}}$. We know from Equation 37 that \mathbf{W} is low rank. Therefore, we can guess a solution of the form

$$\mathbf{W}_{\pm,i} = \pm \mathbf{e}_i \mathbf{x}^\top \quad (40)$$

where the \mathbf{e}_i are the M coordinate vectors. This suggests that we have

$$\mathbf{w}_{\pm,i} = (\sqrt{\mathbf{x} \cdot \mathbf{x}}) \mathbf{e}_i \quad (41)$$

This gives us our final $2M$ eigenmodes.

We can analyze the initial values of the $\tilde{J}(\omega_i)$ as well. The components of the Jacobian can be written as:

$$(\mathbf{J}_v)_i \equiv \frac{\partial f(\mathbf{x})}{\partial \mathbf{v}_i} = \mathbf{U}_{im} \mathbf{x}_m \quad (42)$$

$$(\mathbf{J}_U)_{jm} \equiv \frac{\partial f(\mathbf{x})}{\partial \mathbf{U}_{jm}} = \mathbf{v}_j \mathbf{x}_m \quad (43)$$

From this form, we can deduce that \mathbf{J} is orthogonal to the 0 modes. We can also compute the conserved quantity. Let J_+^2 be the total weight in the positive eigenmodes, and J_-^2 be the total weight in the negative eigenmodes. A direct calculation shows that

$$\omega^{-1} (J_+^2 - J_-^2) = 2f(\mathbf{x}) \quad (44)$$

which implies that $E = 0$.

Therefore, the single-hidden layer linear model on one datapoint is equivalent to the quartic loss model with $E = 0$ and eigenvalues $\pm\sqrt{\mathbf{x} \cdot \mathbf{x}}$.

A.3. Connection to (Bordelon & Pehlevan, 2022)

Since the one-hidden layer linear model has constant \mathbf{Q} , the models in Section F.1 of (Bordelon & Pehlevan, 2022) fall into the quadratic regression class. In the case of Section F.1.1, Equation 67, we can make the mapping to a $D = 1$ model explicit. The dynamics are equivalent to said model with a single eigenvalue ω_0 if we make the identifications

$$\Delta = \tilde{z}, H_y = J_0^2, \gamma_0 = \sqrt{2\omega}, y = -E/2 \quad (45)$$

A.4. Connection to NTH

The Neural Tangent Hierarchy (NTH) equations extend the NTK dynamics to account for changes in the tangent kernel by constructing an infinite sequence of higher order tensors which control the non-linear dynamics of learning (Huang & Yau, 2020). Truncation of the NTH equations at 3rd order is related to, but not the same as the quadratic regression model, as we will show here.

The 3rd order NTH equation describes the change in the tangent kernel $\mathbf{J}\mathbf{J}^\top$. Consider the $D \times D \times D$ -dimensional kernel \mathbf{K}_3 whose elements are given by

$$(\mathbf{K}_3)_{\alpha\beta\gamma} = \frac{\partial^2 \mathbf{z}_\alpha}{\partial \theta_i \partial \theta_j} \mathbf{J}_{i\gamma} \mathbf{J}_{j\beta} + \frac{\partial^2 \mathbf{z}_\beta}{\partial \theta_i \partial \theta_j} \mathbf{J}_{i\gamma} \mathbf{J}_{j\alpha} \quad (46)$$

where repeated indices are summed over. In the NTH, for squared loss the change in the NTK $\mathbf{J}\mathbf{J}^\top$ is given by

$$\frac{d}{dt} (\mathbf{J}\mathbf{J}^\top)_{\alpha\beta} = -\eta (\mathbf{K}_3)_{\alpha\beta\gamma} \mathbf{z}_\gamma \quad (47)$$

For fixed $\mathbf{Q} = \frac{\partial^2 \mathbf{z}}{\partial \theta \partial \theta^\top}$, this equation is identical to the GF equations for the NTK in the quadratic regression model. We note that \mathbf{K}_3 is not constant under the quadratic regression model. Conversely, for fixed \mathbf{K}_3 , $\frac{\partial^2 \mathbf{z}}{\partial \theta \partial \theta^\top}$ is not constant either. Therefore, the two methods can be used to construct different low-order expansions of the dynamics.

B. 2 parameter model

B.1. Progressive sharpening under gradient flow

Given the rescaled variables

$$\tilde{z} = \eta z, \quad T(k) = \eta \mathbf{J} \mathbf{Q}^k \mathbf{J}^\top. \quad (48)$$

we get the dynamical equations

$$\frac{d\tilde{z}}{dt} = -\tilde{z}T(0), \quad \frac{dT(k)}{dt} = -2\tilde{z}T(k+1). \quad (49)$$

We can show that there are initializations which show progressive sharpening at late times - that is, increase in $T(0)$. Consider an initialization where the $T(k)$ are non-negative for even k , and non-positive for odd k . In this case, given the dynamical equations, the $T(k)$ don't change sign. If $\tilde{z} > 0$, then $T(0)$ is non-decreasing at all times.

One example of such an initialization is the case where the eigenvalues of \mathbf{Q} are $\pm\lambda$, and the \mathbf{J} are initialized with more weight in the negative eigenmodes than the positive ones. There are many other families of initializations with this property.

B.2. Derivation of function space dynamical equations

Consider the gradient descent equations:

$$\boldsymbol{\theta}_{t+1} - \boldsymbol{\theta}_t = -\eta \nabla_{\boldsymbol{\theta}} \mathcal{L} = -\frac{\eta}{2} [\boldsymbol{\theta}^\top \mathbf{Q} \boldsymbol{\theta} - E] \mathbf{Q} \boldsymbol{\theta}. \quad (50)$$

We can derive the $\tilde{z} - T$ dynamics as follows. We can re-write the update equation as

$$\boldsymbol{\theta}_{t+1} - \boldsymbol{\theta}_t = -\eta \nabla_{\boldsymbol{\theta}} \mathcal{L} = -\eta z \mathbf{J}^\top. \quad (51)$$

The change in z can be written as

$$\Delta z = \boldsymbol{\theta}^\top \mathbf{Q} \Delta \boldsymbol{\theta} + \frac{1}{2} \Delta \boldsymbol{\theta}^\top \mathbf{Q} \Delta \boldsymbol{\theta} \quad (52)$$

Substituting, we have:

$$\Delta z = -\eta z \mathbf{J} \mathbf{J}^\top + \frac{\eta^2}{2} z^2 \mathbf{J} \mathbf{Q} \mathbf{J}^\top \quad (53)$$

We also have

$$\Delta \mathbf{J} = -\eta z \mathbf{J} \mathbf{Q} \quad (54)$$

We can also write:

$$\Delta(\mathbf{J} \mathbf{Q}^k \mathbf{J}^\top) = -2\eta z \mathbf{J} \mathbf{Q}^{k+1} \mathbf{J}^\top + \eta^2 z^2 \mathbf{J} \mathbf{Q}^{k+2} \mathbf{J}^\top \quad (55)$$

Converting to the $\tilde{z} - T$ coordinates, the gradient descent equations become:

$$\tilde{z}_{t+1} - \tilde{z}_t = -\tilde{z}_t T_t(0) + \frac{1}{2} (\tilde{z}_t^2) T_t(1) \quad (56)$$

$$T_{t+1}(k) - T_t(k) = -\tilde{z}_t (2T_t(k+1) - \tilde{z}_t T_t(k+2)). \quad (57)$$

B.3. Derivation of \tilde{z} - $T(0)$ equations

We can use the conserved quantity \tilde{E} to write the dynamics in terms of \tilde{z} and $T(0)$ only. Without loss of generality, let the eigenvalues are 1 and λ , with $-1 \leq \lambda \leq 1$. (We can achieve this by rescaling \tilde{z} .) Recall the dynamical equations

$$\tilde{z}_{t+1} - \tilde{z}_t = -\tilde{z}_t T_t(0) + \frac{1}{2} (\tilde{z}_t^2) T_t(1) \quad (58)$$

$$T_{t+1}(0) - T_t(0) = -\tilde{z}_t (2T_t(1) - \tilde{z}_t T_t(2)) \quad (59)$$

We will find substitutions for $T(1)$ and $T(2)$ in terms of \tilde{z} and $T(0)$. Recall that we have

$$T(-1) = \tilde{E} + 2\tilde{z} \quad (60)$$

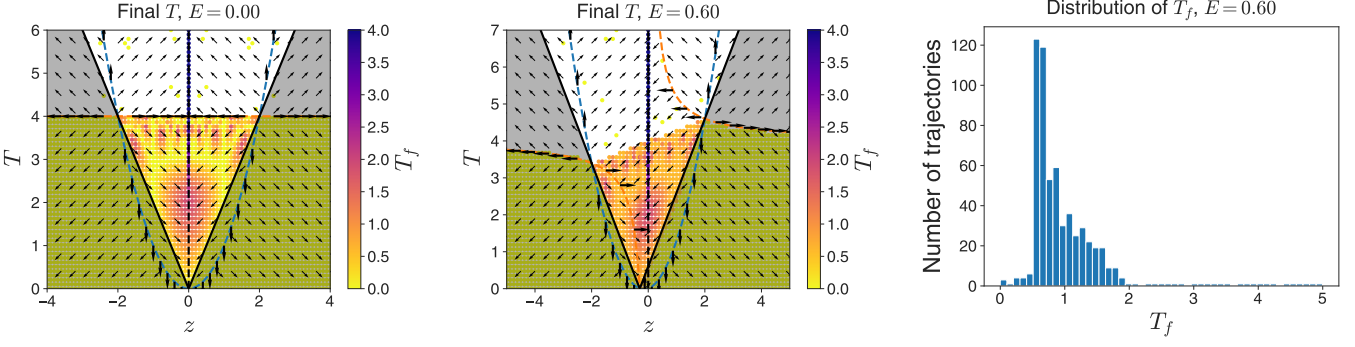


Figure 7. Phase portraits for symmetric model. Arrows indicate signs of changes in z and T , and grey area represents disallowed coordinates. Dynamics are run from an evenly spaced grid of initializations, and the final value of the curvature $T(0)$ is recorded. Nullclines representing $\tilde{z}_{t+1} - \tilde{z}_t = 0$ (blue) and $T_{t+1}(0) - T_t(0) = 0$ (orange) depend on \tilde{E} . Trajectories show progressive sharpening but no edge-of-stability effect (right).

where \tilde{E} is conserved throughout the dynamics (and indeed is a property of the landscape). We will use this definition to solve for $T(1)$ and $T(2)$.

Since $P = 2$, we can write $T(-1) = bT(0) + aT(1)$, for coefficients a and b which are valid for all combinations of \tilde{J} . If $\tilde{J}(\lambda) = 0$, we have $b = 1 - a$. If $\tilde{J}(1) = 0$, we have $1 = \lambda(1 - a) + \lambda^2 a$. Solving, we have:

$$T(-1) = (1 - a)T(0) + aT(1) \text{ for } a = -\frac{1}{\lambda} \quad (61)$$

The restrictions on λ translate to $a \notin (-1, 1)$. In terms of the conserved quantity $\tilde{E} = T(-1) - 2\tilde{z}$, we have:

$$T(-1) = \tilde{E} + 2\tilde{z} \quad (62)$$

In order to convert the dynamics, we need to solve for $T(1)$ and $T(2)$ in terms of $T(0)$ and \tilde{z} . We have:

$$T(1) = \frac{1}{a} (T(-1) + (a - 1)T(0)) = \frac{1}{a} (\tilde{E} + 2\tilde{z} + (a - 1)T(0)) \quad (63)$$

We also have

$$T(2) = T(0) + \left(\frac{1-a}{a^2} \right) (T(0) - \tilde{E} - 2\tilde{z}) \quad (64)$$

This gives us

$$\tilde{z}_{t+1} - \tilde{z}_t = -\tilde{z}_t T_t(0) + \frac{1}{2a} (\tilde{z}_t^2) ((a - 1)T_t(0) + 2\tilde{z}_t + \tilde{E}) \quad (65)$$

$$T_{t+1}(0) - T_t(0) = -\frac{2}{a} \tilde{z}_t (2\tilde{z}_t + \tilde{E} + (a - 1)T_t(0)) + \tilde{z}_t^2 \left[T_t(0) + \left(\frac{1-a}{a^2} \right) (T_t(0) - \tilde{E} - 2\tilde{z}_t) \right] \quad (66)$$

If $\lambda = -\epsilon$ (that is, $a = \epsilon^{-1}$) we recover the equations from the main text.

The non-negativity of \tilde{J}^2 gives us constraints on the values of \tilde{z} and T . For $a > 1$ (small negative second eigenvalue), the constraints are:

$$T > 2\tilde{z} + \tilde{E}, \quad T > -(2\tilde{z} + \tilde{E})/a \quad (67)$$

This is an upward-facing cone with vertex at $\tilde{z} = -\tilde{E}/2$ (Figure 8, left). For $a < -1$, the constraints are

$$-(2\tilde{z} + \tilde{E})/a < T < 2\tilde{z} + \tilde{E} \quad (68)$$

This is a sideways facing cone with vertex at $\tilde{z} = -\tilde{E}/2$ (Figure 8, right). We see that in this case, there is a limited set of values of T to converge to. Indeed, for $\tilde{E} = 0$, there is no convergence except at $T(0) = 0$. This is why we focus on the case of one positive and one negative eigenvalue.

We can also solve for the nullclines - the curves where either $\tilde{z}_{t+1} - \tilde{z}_t = 0$ (blue in Figure 8), or $T_{t+1}(0) - T_t(0) = 0$ (orange in Figure 8). The nullcline $(\tilde{z}, f_{\tilde{z}}(\tilde{z}))$ for \tilde{z} is given by

$$f_{\tilde{z}}(\tilde{z}) = \frac{\tilde{z}(2\tilde{z} + \tilde{E})}{2a - (a-1)\tilde{z}} \quad (69)$$

The nullcline $(\tilde{z}, f_T(\tilde{z}))$ for $T(0)$ is given by

$$f_T(\tilde{z}) = -\frac{(a-1)\tilde{z} - 2a}{(a^2 - a + 1)\tilde{z} - 2a(a-1)}(2\tilde{z} + \tilde{E}) \quad (70)$$

The line $\tilde{z} = 0$ is also a nullcline.

For the symmetric model $\epsilon = 1$, the structure of the nullclines determines the presence or lack of progressive sharpening. For $\tilde{E} = 0$, there is no sharpening; the phase portrait (Figure 7, left) confirms this as the nullcline in $T_t(0)$ divides the space into two halves, one which converges, and the other which doesn't. However, when $\tilde{E} \neq 0$, the nullclines split, and there is a small region where progressive sharpening can occur (Figure 7, middle). However, there is still no edge-of-stability behavior in this case - there is no region where the trajectories cluster near $\lambda_{\max} = 2/\eta$ (Figure 7, right).

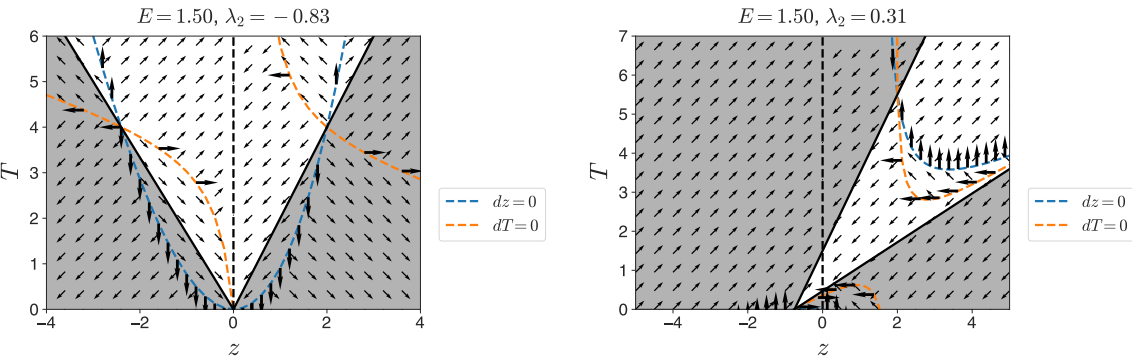


Figure 8. Phase planes of $D = 1, P = 2$ model. Grey region corresponds to parameters forbidden by positivity constraints on $\tilde{J}(\omega_i)^2$. For $\lambda > 0$, allowed region is smaller and intersects $\tilde{z} = 0$ at a small range only. Nullclines can be solved for analytically.

B.4. Two-step dynamics

The two-step difference equations can be derived by iterating Equations 14 and 15. We have

$$\tilde{z}_{t+2} - \tilde{z}_t = p_0(\tilde{z}_t, \epsilon) + p_1(\tilde{z}_t, \epsilon)T_t(0) + p_2(\tilde{z}_t, \epsilon)T_t(0)^2 + p_3(\tilde{z}_t, \epsilon)T_t(0)^3 \quad (71)$$

$$T(0)_{t+2} - T_t(0) = q_0(\tilde{z}_t, \epsilon) + q_1(\tilde{z}_t, \epsilon)T_t(0) + q_2(\tilde{z}_t, \epsilon)T_t(0)^2 + q_3(\tilde{z}_t, \epsilon)T_t(0)^3 \quad (72)$$

Here the p_i and q_i are polynomials in \tilde{z} , maximum 9th order in \tilde{z} and 6th order in ϵ . They can be computed explicitly but we choose to omit the exact forms for now.

Numerical simulation of the dynamics for small ϵ reveals an edge of stability effect (Figure 9). We see that the distribution of final values of T for random initializations has a peak near $T(0) = 2$ (right). By plotting the two-step dynamics, we can see that the two-step nullclines which go in to $T(0) = 2$ almost coincide (left). By studying these nullclines, we will be able to understand the edge of stability effect.

For fixed ϵ , we can solve for the \tilde{z} two-step nullclines ($\tilde{z}_{t+2} - \tilde{z}_t = 0$) and the T nullclines ($T_{t+2}(0) - T_t(0) = 0$) using Cardano's formula to solve for T as a function of \tilde{z} . In particular, each nullcline equation has a solution that goes through $\tilde{z} = 0, T(0) = 2$, independent of ϵ . This is the family of solutions that we will focus on.

Let $(\tilde{z}, f_{\tilde{z},\epsilon}(\tilde{z}))$ be the nullcline of \tilde{z} , and let $(\tilde{z}, f_{T,\epsilon}(\tilde{z}))$ be the nullcline of $T(0)$. We will show that the T values of the nullclines, as a function of \tilde{z} and ϵ , is differentiable around $\tilde{z} = 0, \epsilon = 0$.

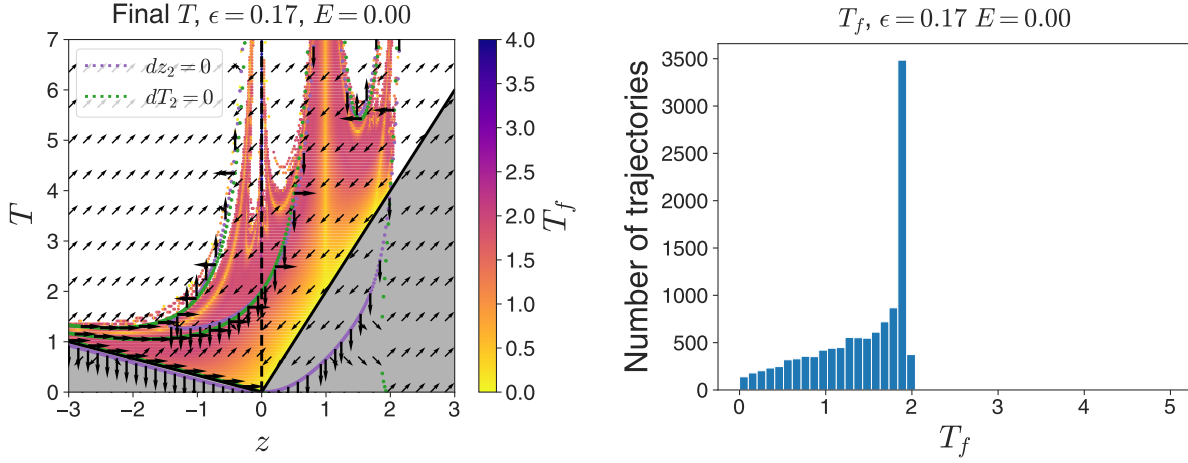


Figure 9. Phase portraits for $\epsilon = 0.17$, $\tilde{E} = 0$. Arrows indicate signs of changes in two step dynamics of \tilde{z} and $T(0)$ (left), and grey area represents disallowed coordinates. Nullclines representing $\tilde{z}_{t+2} - \tilde{z}_t = 0$ (purple) and $T_{t+2}(0) - T_t(0) = 0$ (green) going in to $T(0) = 2$ almost overlap. Final $T(0)$ for initializations taken uniformly over $\tilde{z} - T(0)$ space show a peak near $T(0) = 2$ (right).

The nullclines are defined by the implicit equations

$$0 = 6\tilde{z}^3\epsilon - 2T\tilde{z} - 3T\tilde{z}^2(\epsilon - 1) - T\tilde{z}^3(\epsilon + 2)(2\epsilon + 1) + T^2\tilde{z} + \frac{7}{2}T^2\tilde{z}^2(\epsilon - 1) + \frac{1}{2}T^2\tilde{z}^3(9\epsilon^2 - 10\epsilon + 9) - \frac{1}{2}T^3\tilde{z}^2(\epsilon - 1) - \frac{1}{2}T^3\tilde{z}^3(3\epsilon^2 - 4\epsilon + 3) + O(\tilde{z}^4) \quad (73)$$

$$0 = -8\tilde{z}^2\epsilon - 12\tilde{z}^3(\epsilon - 1)\epsilon + 4T\tilde{z}(\epsilon - 1) + 2T\tilde{z}^2(3\epsilon^2 - \epsilon + 3) + 4T\tilde{z}^3(\epsilon - 1)(\epsilon^2 + 4\epsilon + 1) - 2T^2\tilde{z}(\epsilon - 1) - T^2\tilde{z}^2(7\epsilon^2 - 8\epsilon + 7) - T^2\tilde{z}^3(\epsilon - 1)(9\epsilon^2 - \epsilon + 9) + T^3\tilde{z}^2(\epsilon^2 - \epsilon + 1) + T^3\tilde{z}^3(\epsilon - 1)(3\epsilon^2 - \epsilon + 3) + O(\tilde{z}^4) \quad (74)$$

We omit the higher order terms for now in anticipation of differentiating at $\tilde{z} = 0$ to use the implicit function theorem. Dividing by \tilde{z} , we have the equations

$$0 = 6\tilde{z}^2\epsilon - 2T - 3T\tilde{z}(\epsilon - 1) - T\tilde{z}^2(\epsilon + 2)(2\epsilon + 1) + T^2 + \frac{7}{2}T^2\tilde{z}(\epsilon - 1) + \frac{1}{2}T^2\tilde{z}^2(9\epsilon^2 - 10\epsilon + 9) - \frac{1}{2}T^3\tilde{z}(\epsilon - 1) - \frac{1}{2}T^3\tilde{z}^2(3\epsilon^2 - 4\epsilon + 3) + O(\tilde{z}^3) \quad (75)$$

$$0 = -8\tilde{z}\epsilon - 12\tilde{z}^2(\epsilon - 1)\epsilon + 4T(\epsilon - 1) + 2T\tilde{z}(3\epsilon^2 - \epsilon + 3) + 4T\tilde{z}^2(\epsilon - 1)(\epsilon^2 + 4\epsilon + 1) - 2T^2(\epsilon - 1) - T^2\tilde{z}(7\epsilon^2 - 8\epsilon + 7) - T^2\tilde{z}^2(\epsilon - 1)(9\epsilon^2 - \epsilon + 9) + T^3\tilde{z}(\epsilon^2 - \epsilon + 1) + T^3\tilde{z}^2(\epsilon - 1)(3\epsilon^2 - \epsilon + 3) + O(\tilde{z}^3) \quad (76)$$

We immediately see that $\tilde{z} = 0, T = 2$ solves both equations for all ϵ . Let $w(\epsilon, \tilde{z}, T)$ and $v(\epsilon, \tilde{z}, T)$ be the right hand sides of Equations 75 and 76 respectively. We have

$$\frac{\partial w}{\partial T} \Big|_{(0,0,2)} = 2, \quad \frac{\partial v}{\partial T} \Big|_{(0,0,2)} = 4 \quad (77)$$

In both cases the derivative is invertible. Therefore, $f_{\tilde{z}, \epsilon}(\tilde{z})$ and $f_{T, \epsilon}(\tilde{z})$ are continuously differentiable in both \tilde{z} and ϵ in some neighborhood of 0. In fact, since w and v are analytic in all three arguments, $f_{\tilde{z}, \epsilon}(\tilde{z})$ and $f_{T, \epsilon}(\tilde{z})$ are analytic as well.

We can use the analyticity to solve for the low-order structure of the nullclines. One way to compute the values of the derivatives is to define the nullclines as formal power series:

$$f_{\tilde{z}}(\tilde{z}) = 2 + \sum_{j=1}^{\infty} \sum_{k=1}^{\infty} a_{j,k} \epsilon^j \tilde{z}^k \quad (78)$$

$$f_T(\tilde{z}) = 2 + \sum_{j=1}^{\infty} \sum_{k=1}^{\infty} b_{j,k} \epsilon^j \tilde{z}^k \quad (79)$$

We can then solve for the first few terms of the series using Equations 75 and 76. From this procedure, we have:

$$f_{\tilde{z},\epsilon}(\tilde{z}) = 2 + 2(1-\epsilon)\tilde{z} + 2(1-\epsilon+\epsilon^2)\tilde{z}^2 + O(\tilde{z}^3) \quad (80)$$

$$f_{T,\epsilon}(\tilde{z}) = 2 - \frac{(2-3\epsilon+2\epsilon^2)}{1-\epsilon}\tilde{z} + \frac{1}{2}(4-\epsilon+4\epsilon^2)\tilde{z}^2 + O(\tilde{z}^3) \quad (81)$$

The difference $f_{\Delta,\epsilon}(\tilde{z})$ between the two is:

$$f_{\Delta}(\tilde{z}) \equiv f_{\tilde{z}}(\tilde{z}) - f_T(\tilde{z}) = -\frac{\epsilon}{1-\epsilon}\tilde{z} - \frac{3}{2}\epsilon\tilde{z}^2 + O(\tilde{z}^3) \quad (82)$$

As ϵ decreases, for the low order terms the distance between the nullclines also decreases.

We can show that the difference goes as ϵ . The one-step dynamical equations for $\epsilon = 0$ are

$$\tilde{z}_{t+1} - \tilde{z}_t = -\tilde{z}_t T_t(0) + \frac{1}{2}\tilde{z}_t^2 T_t(0) \quad (83)$$

$$T_{t+1}(0) - T_t(0) = -2\tilde{z}_t T_t(0) + z_t^2 T_t(0) \quad (84)$$

Therefore, $\Delta\tilde{z} = 2\Delta T$. This means that both the one step AND two-step nullclines are identical. Since $f_{\tilde{z},0}(\tilde{z}) = f_{T,0}(\tilde{z})$, and both are differentiable with respect to ϵ , we have:

$$f_{\tilde{z},\epsilon}(\tilde{z}) - f_{T,\epsilon}(\tilde{z}) = \epsilon f_{\Delta,\epsilon}(\tilde{z}) \quad (85)$$

for some function $f_{\Delta,\epsilon}(\tilde{z})$ which is analytic in ϵ and \tilde{z} in a neighborhood around $(0,0)$.

B.5. Two-step dynamics of y

It is useful to define dynamical equations in coordinates (\tilde{z}, y) where y is the difference between $T(0)$ and the \tilde{z} nullcline:

$$y \equiv T(0) - f_{\tilde{z},\epsilon}(\tilde{z}) \quad (86)$$

To lowest order in \tilde{z} and ϵ we have

$$y = T(0) - 2 - 2(1-\epsilon)\tilde{z} - 2(1-\epsilon+\epsilon^2)\tilde{z}^2 + O(\tilde{z}^3) \quad (87)$$

We note that $y = 0$, at $\tilde{z} = 0$ corresponds to $T(0) = 2$. y near but slightly less than 0 is equivalent to edge-of-stability behavior. For positive \tilde{z} , $y = 0$ implies $T(0) > 2$.

We can write the dynamics of \tilde{z} and y . The dynamics for \tilde{z} are given by:

$$\tilde{z}_{t+2} - \tilde{z}_t = p_0(\tilde{z}_t, \epsilon) + p_1(\tilde{z}_t, \epsilon)(y_t + f_{\tilde{z},\epsilon}(\tilde{z}_t)) + p_2(\tilde{z}_t, \epsilon)(y_t + f_{\tilde{z},\epsilon}(\tilde{z}_t))^2 + p_3(\tilde{z}_t, \epsilon)(y_t + f_{\tilde{z},\epsilon}(\tilde{z}_t))^3 \quad (88)$$

We know that the right hand side of this equation is analytic in \tilde{z} , ϵ , and (trivially) y as well. By evaluating the multiple continuous derivatives of f , we can write:

$$\tilde{z}_{t+2} - \tilde{z}_t = 2y_t \tilde{z}_t + y_t^2 \tilde{z}_t f_{1,\epsilon}(\tilde{z}_t, y_t) + y_t \tilde{z}_t^2 f_{2,\epsilon}(\tilde{z}_t) \quad (89)$$

880 Here, $f_{1,\epsilon}$ and $f_{2,\epsilon}$ are analytic in \tilde{z}, ϵ , and y in some neighborhood around 0.

881 This means that we have the bounds

$$883 |f_{1,\epsilon}(\tilde{z}, y)| < F_1, |f_{2,\epsilon}(\tilde{z}, y)| < F_2 \quad (90)$$

884 for $(\tilde{z}, \epsilon, y) \in [-\tilde{z}_d, \tilde{z}_d] \times [0, \epsilon_d] \times [-y_d, y_d]$ for some non-negative constants F_1 and F_2 . Note that this bound is independent
885 of ϵ .

886 Now we consider the dynamics of y . We have:

$$889 y_{t+2} - y_t = T_{t+2}(0) - T_t(0) - f_{\tilde{z},\epsilon}(\tilde{z}_{t+2}) + f_{\tilde{z},\epsilon}(\tilde{z}_t) \quad (91)$$

890 Since $\lim_{\tilde{z} \rightarrow 0, y \rightarrow 0} \tilde{z}_{t+2} = 0$, $f_{\tilde{z},\epsilon}(\tilde{z}_{t+2})$ is analytic in some neighborhood of $(0, 0, 0)$. Therefore $y_{t+2} - y_t$ is analytic as
891 well. Substituting, we have

$$892 y_{t+2} - y_t = q_0(\tilde{z}_t, \epsilon) + q_1(\tilde{z}_t, \epsilon)[y + f_{\tilde{z},\epsilon}(\tilde{z})] + q_2(\tilde{z}_t, \epsilon)[y + f_{\tilde{z},\epsilon}(\tilde{z})]^2 + q_3(\tilde{z}_t, \epsilon)[y + f_{\tilde{z},\epsilon}(\tilde{z})]^3 \\ 893 - f_{\tilde{z},\epsilon}(\tilde{z}_t + 2y_t \tilde{z}_t + y_t^2 \tilde{z}_t f_{1,\epsilon}(\tilde{z}_t, y_t) + y_t \tilde{z}_t^2 f_{2,\epsilon}(\tilde{z}_t)) + f_{\tilde{z},\epsilon}(\tilde{z}_t) \quad (92)$$

894 If we write $f_{\tilde{z},\epsilon}(\tilde{z}) = f_{T,\epsilon}(\tilde{z}) + \epsilon f_{\Delta,\epsilon}(\tilde{z})$, then we can write:

$$895 y_{t+2} - y_t = q_0(\tilde{z}_t, \epsilon) + q_1(\tilde{z}_t, \epsilon)[f_{T,\epsilon}(\tilde{z})] + q_2(\tilde{z}_t, \epsilon)[f_{T,\epsilon}(\tilde{z})]^2 + q_3(\tilde{z}_t, \epsilon)[f_{T,\epsilon}(\tilde{z})]^3 \\ 896 - 2q_2(\tilde{z}_t, \epsilon)[f_{T,\epsilon}(\tilde{z})(y + \epsilon f_{\Delta,\epsilon}(\tilde{z}))] + 3q_3(\tilde{z}_t, \epsilon)[(f_{T,\epsilon}(\tilde{z}))(y + \epsilon f_{\Delta,\epsilon}(\tilde{z}))^2 + (f_{T,\epsilon}(\tilde{z}))^2(y + \epsilon f_{\Delta,\epsilon}(\tilde{z}))] \\ 897 q_0(\tilde{z}_t, \epsilon) + q_1(\tilde{z}_t, \epsilon)[y + \epsilon f_{\Delta,\epsilon}(\tilde{z})] + q_2(\tilde{z}_t, \epsilon)[y + \epsilon f_{\Delta,\epsilon}(\tilde{z})]^2 + q_3(\tilde{z}_t, \epsilon)[y + \epsilon f_{\Delta,\epsilon}(\tilde{z})]^3 \\ 898 - f_{\tilde{z},\epsilon}(\tilde{z}_t + 2y_t \tilde{z}_t + y_t^2 \tilde{z}_t f_{1,\epsilon}(\tilde{z}_t, y_t) + y_t \tilde{z}_t^2 f_{2,\epsilon}(\tilde{z}_t)) + f_{\tilde{z},\epsilon}(\tilde{z}_t) \quad (93)$$

899 By the definition of the nullclines, the first four terms vanish. Once again using the differentiability of the nullclines, as well
900 as $f_{1,\epsilon}$ and $f_{2,\epsilon}$, we can rewrite the dynamics in terms of the expansion:

$$901 y_{t+2} - y_t = -2(4 - 3\epsilon + 4\epsilon^2)y_t \tilde{z}_t^2 - 4\epsilon \tilde{z}_t^2 + y_t^2 \tilde{z}_t^2 g_{1,\epsilon}(\tilde{z}_t, y_t) + \epsilon \tilde{z}_t^3 g_{2,\epsilon}(\tilde{z}_t) \quad (94)$$

902 Here $g_{1,\epsilon}$ and $g_{2,\epsilon}$ are analytic near zero in \tilde{z}, y , and ϵ . We have the bounds

$$903 |g_{1,\epsilon}(\tilde{z}, y)| < G_1, |g_{1,\epsilon}(\tilde{z}, y)| < G_2 \quad (95)$$

904 for $(\tilde{z}, \epsilon, y) \in [-\tilde{z}_d, \tilde{z}_d] \times [0, \epsilon_d] \times [-y_d, y_d]$ for some non-negative constants G_1 and G_2 . This bound is also independent
905 of ϵ .

906 We can summarize these bounds in the following lemma:

907 **Lemma B.1.** Define $y = T - f_{\tilde{z}}(\tilde{z})$. The two step dynamics of \tilde{z} and y are given by

$$908 \tilde{z}_{t+2} - \tilde{z}_t = 2y_t \tilde{z}_t + y_t^2 \tilde{z}_t f_{1,\epsilon}(\tilde{z}_t, y_t) + y_t \tilde{z}_t^2 f_{2,\epsilon}(\tilde{z}_t) \quad (96)$$

$$910 y_{t+2} - y_t = -2(4 - 3\epsilon + 4\epsilon^2)y_t \tilde{z}_t^2 - 4\epsilon \tilde{z}_t^2 + y_t^2 \tilde{z}_t^2 g_{1,\epsilon}(\tilde{z}_t, y_t) + \epsilon \tilde{z}_t^3 g_{2,\epsilon}(\tilde{z}_t, y_t) \quad (97)$$

911 Where $f_{1,\epsilon}, f_{2,\epsilon}, g_{1,\epsilon}, g_{2,\epsilon}$ are all analytic in \tilde{z}, y , and ϵ . Additionally, there exist positive \tilde{z}_c, y_c , and ϵ_c such that

$$912 |f_{1,\epsilon}(\tilde{z}, y)| < F_1, |f_{2,\epsilon}(\tilde{z}, y)| < F_2, |g_{1,\epsilon}(\tilde{z}, y)| < G_1, |g_{1,\epsilon}(\tilde{z}, y)| < G_2 \quad (98)$$

913 for all $(\tilde{z}, \epsilon, y) \in [-\tilde{z}_d, \tilde{z}_d] \times [0, \epsilon_d] \times [-y_d, y_d]$, where F_1, F_2, G_1 , and G_2 are all non-negative constants.

914 We can use this Lemma to analyze the dynamics for small fixed ϵ , for small initializations of \tilde{z}, y . The control of the higher
915 order terms will allow for an analysis which focuses on the effects of the lower order terms.

935 **B.6. Proof of Theorem 3.1**

 936 Using Lemma B.1, the dynamics in \tilde{z} and y can be written as:

938
$$\tilde{z}_{t+2} - \tilde{z}_t = 2y_t \tilde{z}_t + y_t^2 \tilde{z}_t f_{1,\epsilon}(\tilde{z}_t, y_t) + y_t \tilde{z}_t^2 f_{2,\epsilon}(\tilde{z}_t) \quad (99)$$

941
$$y_{t+2} - y_t = -2(4 - 3\epsilon + 4\epsilon^2)y_t \tilde{z}_t^2 - 4\epsilon \tilde{z}_t^2 + y_t^2 \tilde{z}_t^2 g_{1,\epsilon}(\tilde{z}_t, y_t) + \epsilon \tilde{z}_t^3 g_{2,\epsilon}(\tilde{z}_t, y_t) \quad (100)$$

 942 Let $\epsilon < \epsilon_d$. Then we can use the bounds from Lemma B.1 to control the contributions of the higher order terms to the dynamics:

 943 **Lemma B.2.** *Given constants $A > 0$ and $B > 0$, there exist \tilde{z}_c and y_c such that for $\tilde{z} \in [0, 2\tilde{z}_c]$, $y \in [-y_c, y_c]$, we have the bounds:*

947
$$|y^2 \tilde{z} f_{1,\epsilon}(\tilde{z}, y) + y \tilde{z}^2 f_{2,\epsilon}(\tilde{z})| \leq A |2y \tilde{z}| \quad (101)$$

949
$$|y^2 \tilde{z}^2 g_{1,\epsilon}(\tilde{z}, y)| \leq \frac{B}{8} |2(4 - 3\epsilon + 4\epsilon^2)y \tilde{z}^2| \quad (102)$$

952
$$|\epsilon \tilde{z}^3 g_{2,\epsilon}(\tilde{z}, y)| \leq \frac{B}{4} |4\epsilon \tilde{z}^2| \quad (103)$$

 954 *Proof.* We begin by the following decomposition:

956
$$|y^2 \tilde{z} f_{1,\epsilon}(\tilde{z}, y) + y \tilde{z}^2 f_{2,\epsilon}(\tilde{z})| \leq |y^2 \tilde{z} f_{1,\epsilon}(\tilde{z}, y)| + |y \tilde{z}^2 f_{2,\epsilon}(\tilde{z})| \quad (104)$$

 958 From Lemma B.1, there exists a region $[-\tilde{z}_d, \tilde{z}_d] \times [0, \epsilon_d] \times [-y_d, y_d]$ where the magnitudes of $f_{1,\epsilon}$, $f_{2,\epsilon}$, $g_{1,\epsilon}$, and $g_{2,\epsilon}$ are bounded by F_1 , F_2 , G_1 , and G_2 respectively.

961
$$|y^2 \tilde{z} f_{1,\epsilon}(\tilde{z}, y) + y \tilde{z}^2 f_{2,\epsilon}(\tilde{z})| \leq F_1 y^2 \tilde{z} + F_2 y \tilde{z}^2 \quad (105)$$

964
$$|y^2 \tilde{z}^2 g_{1,\epsilon}(\tilde{z}, y)| \leq G_1 y^2 \tilde{z}^2 \quad (106)$$

966
$$|\tilde{z}^3 g_{2,\epsilon}(\tilde{z}, y)| \leq G_2 \tilde{z}^3 \quad (107)$$

 968 Define \tilde{z}_c and y_c as

969
$$y_c = \min(A/F_1, B/2G_1, y_d), \quad \tilde{z}_c = \min(A/2F_2, B/2G_2, y_c) \quad (108)$$

 971 The desired bounds follow immediately. \square

 972 We consider an initialization (\tilde{z}_0, y_0) such that $\tilde{z}_0 \leq \tilde{z}_c$ and $y_0 \leq y_c$, and $y_0 \leq \tilde{z}_0^2$. Armed with Lemma B.2, we can analyze the dynamics. There are two phases; in the first phase, \tilde{z} is increasing, and y is decreasing. The first phase ends when y becomes negative for the first time - reaching a value of $O(\epsilon)$. In the second phase, \tilde{z} is decreasing, and y stays negative and $O(\epsilon)$.

 977 **B.6.1. PHASE ONE**

 979 Let t_{sm} be the time such that for $t \leq t_{sm}$, $\tilde{z}_t \leq 2\tilde{z}_0$. (We will later show that $\tilde{z}_t \leq 2\tilde{z}_0$ over the whole dynamics.) For $t \leq t_{sm}$, using Lemma B.2, the change in \tilde{z} can be bounded from below by

982
$$\tilde{z}_{t+2} - \tilde{z}_t \geq 2y_t \tilde{z}_t (1 - A) \quad (109)$$

 984 Therefore at initialization, \tilde{z} is increasing. It remains increasing until y_t becomes negative, or $\tilde{z}_t \geq 2\tilde{z}_0$. We want to show that y_t becomes negative before $\tilde{z}_t \geq 2\tilde{z}_0$.

 986 For any $t \leq t_{sm}$, Lemma B.2 gives the following upper bound on $y_{t+2} - y_t$:

988
$$y_{t+2} - y_t \leq -(8 - B)y_t \tilde{z}_t^2 - (4 - B)\epsilon \tilde{z}_t^2 \quad (110)$$

990 Let t_- be the first time that y_t becomes negative. Since \tilde{z}_t is increasing for $t \leq t_-$, we have

$$991 \quad 992 \quad 993 \quad 994 \quad 995 \quad 996 \quad 997 \quad 998 \quad 999 \quad y_{t+2} - y_t \leq -(8 - B)y_t\tilde{z}_0^2 - (4 - B)\epsilon\tilde{z}_0^2 \quad (111)$$

This gives us the following bound on y_t :

$$995 \quad 996 \quad 997 \quad 998 \quad 999 \quad y_t \leq y_0 e^{-(8-B)\tilde{z}_0^2 t} \quad (112)$$

valid for $t \leq t_-$ and $t \leq t_{sm}$.

We will now show that $t_- < t_{sm}$. Suppose that $t_{sm} \leq t_-$. Then at $t_{sm} + 2$, $\tilde{z}_{t_{sm}+2} > 2\tilde{z}_0$ for the first time. Summing the bound in Equation 109, we have:

$$1000 \quad 1001 \quad 1002 \quad 1003 \quad \tilde{z}_{t_{sm}+2} - \tilde{z}_0 \leq \sum_{t=0}^{t_{sm}} 2y_t\tilde{z}_t(1+A) \leq 4\tilde{z}_0(1+A) \sum_{t=0}^{t_{sm}} y_t \quad (113)$$

1004 where the second bound comes from the definition of t_{sm} . Using our bound on y_t , we have:

$$1005 \quad 1006 \quad 1007 \quad 1008 \quad \tilde{z}_{t_{sm}+2} - \tilde{z}_0 \leq 4\tilde{z}_0(1+A) \sum_{s=0}^{t_{sm}} y_0 e^{-(8-B)\tilde{z}_0^2 s} \leq \frac{(1+A)}{2} \frac{y_0}{\tilde{z}_0} \quad (114)$$

1009 Since $y_0 \leq \tilde{z}_0^2$, $\tilde{z}_{t_{sm}+2} \leq 2\tilde{z}_0$. However, by assumption $\tilde{z}_{t_{sm}+2} > 2\tilde{z}_0$. We arrive at a contradiction; t_{sm} is not less than or 1010 equal to t_- .

1011 There are three possibilities: the first is that t_- is well-defined, and $t_- < t_{sm}$. Another possibility is that t_- is not 1012 well-defined - that is, y_t never becomes negative. In this case the bounds we derived are valid for all t . Therefore using 1013 Equation 112, there exists some time t_ϵ where $y_{t_\epsilon} < (4 - B)\epsilon\tilde{z}_0^2$. Then, using Equation 111 we have $y_{t_\epsilon+2} < 0$. Therefore, 1014 we conclude that t_- is finite and less than t_{sm} .

1015 Since the well defined value $t_- < t_{sm}$, when y first becomes negative, $\tilde{z}_{t_-} \leq 2\tilde{z}_0$. This means that we can continue to 1016 apply the bounds from Lemma B.2 at the start of the next phase. At $t = t_- - 2$, applying Lemma B.2 and $\tilde{z}_{t_-} \leq 2\tilde{z}_0$, we 1017 have

$$1018 \quad 1019 \quad 1020 \quad y_{t_-} - y_{t_- - 2} \geq -4(8 + B)y_{t_- - 2}\tilde{z}_0^2 - 4(4 + B)\epsilon\tilde{z}_0^2 \quad (115)$$

1021 which gives us $y_{t_-} \geq -4(4 + B)\epsilon\tilde{z}_0^2$. This concludes the first phase. To summarize we have

$$1022 \quad 1023 \quad -4(4 + B)\epsilon\tilde{z}_0^2 < y_{t_-} \leq 0, \quad \tilde{z}_{t_-} \leq 2\tilde{z}_0 \quad (116)$$

1024 B.6.2. PHASE TWO

1025 Now consider the second phase of the dynamics. We will show that y remains negative and $O(\epsilon)$, and \tilde{z} decreases to 0. 1026 While y is negative, \tilde{z} decreases. While $y \geq -y_0$, from Lemma B.2 we have

$$1027 \quad 1028 \quad \tilde{z}_{t+2} - \tilde{z}_t \leq (1 - A)2y_t\tilde{z}_t \quad (117)$$

1029 Therefore as long as $-y_0 \leq y < 0$, \tilde{z}_t is decreasing. If this is true for all subsequent t , \tilde{z}_0 will converge to 0.

1030 We will now show that y remains negative and $O(\epsilon)$, concluding the proof. Let $y^* = -\frac{\epsilon}{2 - (3/2)\epsilon + 2\epsilon^2}$. We can re-write the 1031 dynamical equation for y as

$$1032 \quad 1033 \quad 1034 \quad y_{t+2} - y_t = -2(4 - 3\epsilon + 4\epsilon^2)\tilde{z}_t^2(y_t - y^*) + y_t^2\tilde{z}_t^2g_1(\tilde{z}_t, y_t) + \tilde{z}_t^3g_2(\tilde{z}_t, y_t) \quad (118)$$

1035 Applying Lemma B.2 to the higher order terms, we have:

$$1036 \quad 1037 \quad 1038 \quad y_{t+2} - y_t \leq -2(4 - 3\epsilon + 4\epsilon^2)\tilde{z}_t^2(y_t - y^*) + B(|y_t| + \epsilon)\tilde{z}_t^2 \quad (119)$$

$$1039 \quad 1040 \quad 1041 \quad y_{t+2} - y_t \geq -2(4 - 3\epsilon + 4\epsilon^2)\tilde{z}_t^2(y_t - y^*) - B(|y_t| + \epsilon)\tilde{z}_t^2 \quad (120)$$

1042 These inequalities are valid as long as $|y_t| < y_c$.

1045 We can use these bounds to construct two auxiliary sequences u_t and v_t such that $u_t \leq y_t \leq v_t$. Let $u_{t-} = v_{t-} = y_{t-}$. The
1046 dynamics of u_t and v_t are given by

$$1047 \quad u_{t+2} - u_t = -8\tilde{z}_t^2(u_t - u^*) \quad (121)$$

$$1049 \quad v_{t+2} - v_t = -8\tilde{z}_t^2(v_t - v^*) \quad (122)$$

1050 where $u^* = y^* - 4B\tilde{z}_{t-}^2\epsilon$ and $v^* = y^* + 4B\tilde{z}_{t-}^2\epsilon$.

1052 We first analyze the dynamics of v_t . Consider the coordinate δ_t defined by the equation

$$1054 \quad v_t = -(1 + \delta_t)v^* \quad (123)$$

1056 The dynamics of δ_t are given by

$$1057 \quad \delta_{t+2} = (1 - 8\tilde{z}_t^2)\delta_t \quad (124)$$

1059 Since $8\tilde{z}_t^2 < 1$, δ_t is strictly decreasing in magnitude. We can bound δ_t from above by

$$1060 \quad | \delta_t | \leq \exp \left(-8 \sum_{s=t-}^t \tilde{z}_s^2 \right) | \delta_{t-} | \quad (125)$$

1064 Since δ starts negative, and is decreasing in magnitude, we know that $v_t > v^*$, which implies $y_t > v^*$ as well. From the
1065 dynamical equations for \tilde{z}_t , we can bound \tilde{z}_t by

$$1066 \quad \tilde{z}_t \geq 2e^{-\epsilon t}\tilde{z}_0 \quad (126)$$

1068 by choosing sufficiently small B (uniformly with respect to ϵ). Substitution gives us the following bound on δ_t :

$$1069 \quad | \delta_t | \leq \exp \left(-8 \sum_{s=t-}^t 4e^{-2\epsilon s}\tilde{z}_0^2 \right) | \delta_{t-} | \quad (127)$$

1073 Using the integral approximation for the sum, the bound becomes

$$1075 \quad | \delta_t | \leq \exp \left(-32\tilde{z}_0^2 \int_0^t e^{-2\epsilon s} ds \right) | \delta_{t-} | = \exp \left(-16\tilde{z}_0^2/\epsilon(1 - e^{-2\epsilon t}) \right) | \delta_{t-} | \quad (128)$$

1078 From the dynamical equations, $-1 \leq \delta_{t-} \leq 0$. In the limit of large t we have

$$1080 \quad \lim_{t \rightarrow \infty} | \delta_t | \leq \exp \left(-16\tilde{z}_0^2/\epsilon \right) | \delta_{t-} | \quad (129)$$

1082 If we have the condition

$$1083 \quad 16\tilde{z}_0^2/\epsilon \geq -\log(\epsilon) \quad (130)$$

1084 then $\lim_{t \rightarrow \infty} | \delta_t | \leq \epsilon^2$. Therefore under the assumption $\tilde{z}_0^2 \geq \epsilon \log(\epsilon^{-1})/16$, we have $\lim_{t \rightarrow \infty} v_t = -\epsilon/2 + O(B\epsilon^2 \log(\epsilon^{-1}))$. Note that requiring $\tilde{z}_0^2 \geq \epsilon_c \log(\epsilon_c^{-1})/16$ ensures that the condition is met for all $\epsilon \leq \epsilon_c$. If
1086 $\epsilon_c \log(\epsilon_c^{-1})/16 \leq \tilde{z}_c^2$, then by the uniformity of the bounds we can reduce ϵ_c until all the bounds are simultaneously
1087 met.

1089 An analogous argument shows that $\lim_{t \rightarrow \infty} u_t = -\epsilon/2 - O(B\epsilon^2 \log(\epsilon^{-1}))$, under the same conditions on \tilde{z}_0 . From the
1090 bound $u_t \leq y_t \leq v_t$, we can conclude that

$$1092 \quad \lim_{t \rightarrow \infty} y_t = -\epsilon/2 + \delta^*, \quad |\delta^*| \leq B\epsilon^2 \log(\epsilon^{-1}) \quad (131)$$

1093 under our assumptions.

1095 Now we can prove the statement of Theorem 3.1. Given a model with $\epsilon \leq \epsilon_c$, there is a continuous mapping between $\theta - \eta$
1096 space and $\tilde{z} - y$ space. Since the region $[\epsilon_c \log(\epsilon_c^{-1}), \tilde{z}_c] \times [0, y_c]$ in $\tilde{z} - y$ space displays edge-of-stability behavior for
1097 ϵ -independent \tilde{z}_c and y_c . This corresponds to an ϵ -independent neighborhood U in $(\tilde{z}_0, \eta\lambda_{max}, \eta)$ as well. This concludes
1098 the proof. \square

1099

This result can be confirmed numerically by running the dynamical equations from a variety of initializations, computing the median eigenvalue (restricted to the range [1.9, 2.0]), and plotting versus ϵ (Figure 10, left). For comparison, we also plot the limiting value of y for the low-order ODE approximation to the dynamics

$$\dot{\tilde{z}} = 2y\tilde{z} \quad (132)$$

$$\dot{y} = -2(4 - 3\epsilon + 4\epsilon^2)y\tilde{z}^2 - 4\epsilon\tilde{z}^2 \quad (133)$$

where we also obtain the limit $-\epsilon/2 + O(\epsilon^2)$, with much less effort. For small ϵ , both quantities show an $O(\epsilon^2)$ deviation from $2 - \epsilon/2$ (Figure 10, right).

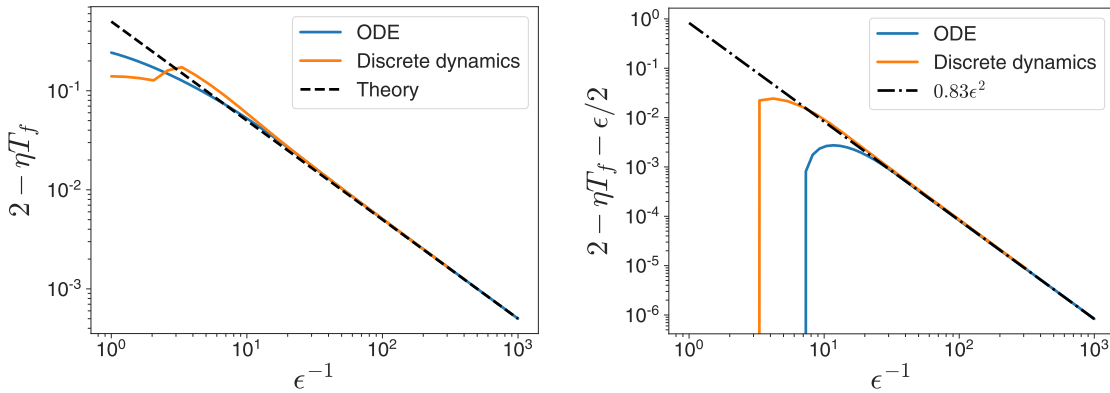


Figure 10. Final values of y , normalized deviation from critical value $T(0) = 2$, for discrete dynamics and ODE approximation. Deviation is well approximated by $\epsilon/2$ over a large range (left). Deviations from $\epsilon/2$ are $O(\epsilon^2)$ (right).

B.7. Parameter space vs. $\tilde{z} - T$ space

Most of our analysis has been focused in the normalized $\tilde{z} - T$ coordinate space. In this section, we confirm that the more usual setup in parameter space is consistent with the normalized coordinate space. In particular, EOS behavior is often described by fixing an initialization, and training with different learning rates - as in Figure 1.

We can plot the dynamics of $T(0)$ for the trajectories from Figure 1. We see that for small learning rates there is convergence to $T(0) < 2$, large learning rates there's divergence, and for intermediate learning rates there is convergence to $2 - \epsilon/2$ (Figure 11).

This confirms that the theorem is useful to describe the more traditional method of discovering and exploring EOS behavior.

C. Quadratic regression model dynamics

We use Einstein summation notation in this section - repeated indices on the right-hand-side of equations are considered to be summed over, unless they show up on the left-hand-side.

C.1. Proof of Theorem 4.1

Let \mathbf{z} , \mathbf{J} , and \mathbf{Q} be initialized with i.i.d. random elements with 0 mean and variance σ_z^2 , σ_J^2 , and 1 respectively. Furthermore, let the distributions be invariant to rotations in both data space and parameter space, and have finite 4th moment.

In order to understand the development of the curvature at early times, we consider coordinates which convert \mathbf{J} into its singular value form. In these coordinates, we can write:

$$\mathbf{J}_{\alpha i} = \begin{cases} 0 & \text{if } \alpha \neq i \\ \sigma_\alpha & \text{if } \alpha = i \end{cases} \quad (134)$$

The singular values σ_α are the square roots of the singular values of the NTK matrix. We assume that they are ordered from largest (σ_1) to smallest in magnitude. By assumption, under this rotation the statistics of \mathbf{z} and \mathbf{Q} are left unchanged.

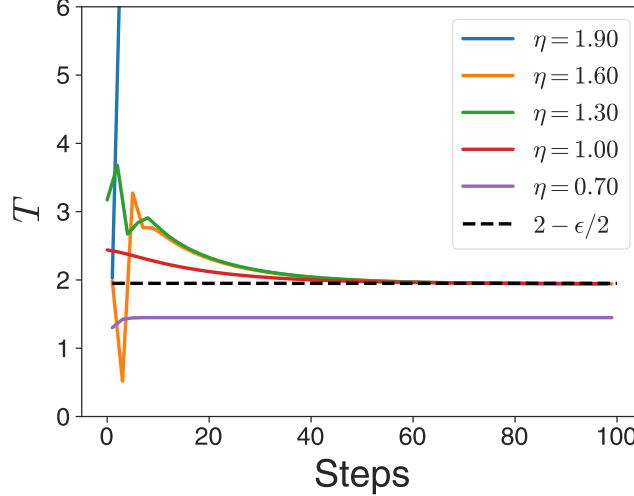


Figure 11. Dynamics of T for trajectories from Figure 1. For small learning rate η , trajectories converge to $T < 2$, and for large learning rates trajectories diverge. For intermediate trajectories, we have EOS behavior, where final T is predicted by Theorem 3.1.

The time derivatives at $t = 0$ can be computed directly in the singular value coordinates. The first derivative is given by

$$\frac{d}{dt}\sigma_\alpha^2 = 2\sigma_\alpha\dot{\sigma}_\alpha \quad (135)$$

Using the diagonal coordinate system, we have

$$E\left[\frac{d}{dt}\sigma_\alpha^2\right] = E[\mathbf{Q}_{\alpha\beta j}\mathbf{J}_{\beta j}\mathbf{z}_\beta] = 0 \quad (136)$$

However, the average second derivative is positive. Calculating, we have:

$$\frac{d^2}{dt^2}\sigma_\alpha^2 = 2(\dot{\sigma}_\alpha^2 + \sigma_\alpha\ddot{\sigma}_\alpha) \quad (137)$$

We can compute the average at initialization. We have:

$$E[\dot{\sigma}_\alpha^2] = E[\mathbf{Q}_{\alpha\beta j}\mathbf{J}_{\beta j}\mathbf{z}_\beta\mathbf{Q}_{\alpha\delta k}\mathbf{J}_{\delta k}\mathbf{z}_\delta] = E[\delta_{\beta\delta}\delta_{jk}\mathbf{J}_{\beta j}\mathbf{J}_{\delta k}\mathbf{z}_\beta\mathbf{z}_\delta] \quad (138)$$

$$E[\dot{\sigma}_\alpha^2] = E[\mathbf{Q}_{\alpha\beta j}\mathbf{J}_{\beta j}\mathbf{z}_\beta\mathbf{Q}_{\alpha\delta k}\mathbf{J}_{\delta k}\mathbf{z}_\delta] = \sum_j E[\mathbf{J}_{\beta j}^2\mathbf{z}_\beta^2] = DP\sigma_J^2\sigma_z^2 \quad (139)$$

To compute the second term, we compute $\ddot{\mathbf{J}}_{\alpha i}$:

$$\ddot{\mathbf{J}}_{\alpha i} = -\mathbf{Q}_{\alpha ij}(\mathbf{J}_{\beta j}\dot{\mathbf{z}}_\beta + \dot{\mathbf{J}}_{\beta j}\mathbf{z}_\beta) \quad (140)$$

Expanding, we have:

$$\ddot{\mathbf{J}}_{\alpha i} = \mathbf{Q}_{\alpha ij}(\mathbf{J}_{\beta j}\mathbf{J}_{\beta k}\mathbf{J}_{\delta k}\mathbf{z}_\delta + \mathbf{Q}_{\beta jk}\mathbf{J}_{\delta k}\mathbf{z}_\delta\mathbf{z}_\beta) \quad (141)$$

In the diagonal coordinates $\mathbf{J}_{\alpha\alpha} = \sigma_\alpha$. This gives us:

$$E[\sigma_\alpha\ddot{\sigma}_\alpha] = E[\sigma_\alpha\mathbf{Q}_{\alpha\alpha j}\mathbf{Q}_{\beta jk}\mathbf{J}_{\delta k}\mathbf{z}_\delta\mathbf{z}_\beta] \quad (142)$$

Averaging over the \mathbf{Q} , we get:

$$E[\sigma_\alpha\ddot{\sigma}_\alpha] = PE[\sigma_\alpha\delta_{\alpha\beta}\delta_{\alpha k}\mathbf{J}_{\delta k}\mathbf{z}_\delta\mathbf{z}_\beta] = E[\sigma_\alpha\mathbf{z}_\alpha\mathbf{z}_\delta\mathbf{J}_{\delta\alpha}] \quad (143)$$

Which evaluates to:

$$E[\sigma_\alpha \ddot{\sigma}_\alpha] = \sigma_z^2 P E[\sigma_\alpha^2] \quad (144)$$

In the limit of large D and P , for fixed ratio D/P , the statistics of the Marchenko-Pastur distribution allow us to compute the derivative of the largest eigenmode as

$$E[\sigma_0 \ddot{\sigma}_0] = \sigma_z^2 \sigma_J^2 P^2 D (1 + \sqrt{D/P})^2 \quad (145)$$

Taken together, this gives us

$$E\left[\frac{d^2 \lambda_{max}}{dt^2}\right] = \sigma_z^2 \sigma_J^2 DP (P(1 + \sqrt{D/P})^2 + 1) \quad (146)$$

We confirm the prediction numerically in Figure 12.

That is, the second derivative of the maximum curvature is positive on average. If we normalize with respect to the eigenvalue scale, in the limit of large D and P we have:

$$E\left[\frac{d^2 \lambda_{max}}{dt^2}\right] / E[\lambda_{max}] = \sigma_z^2 \quad (147)$$

Therefore, increasing σ_z increases the relative curvature of the λ_{max} trajectory. This gives us the proof of Theorem 4.1.

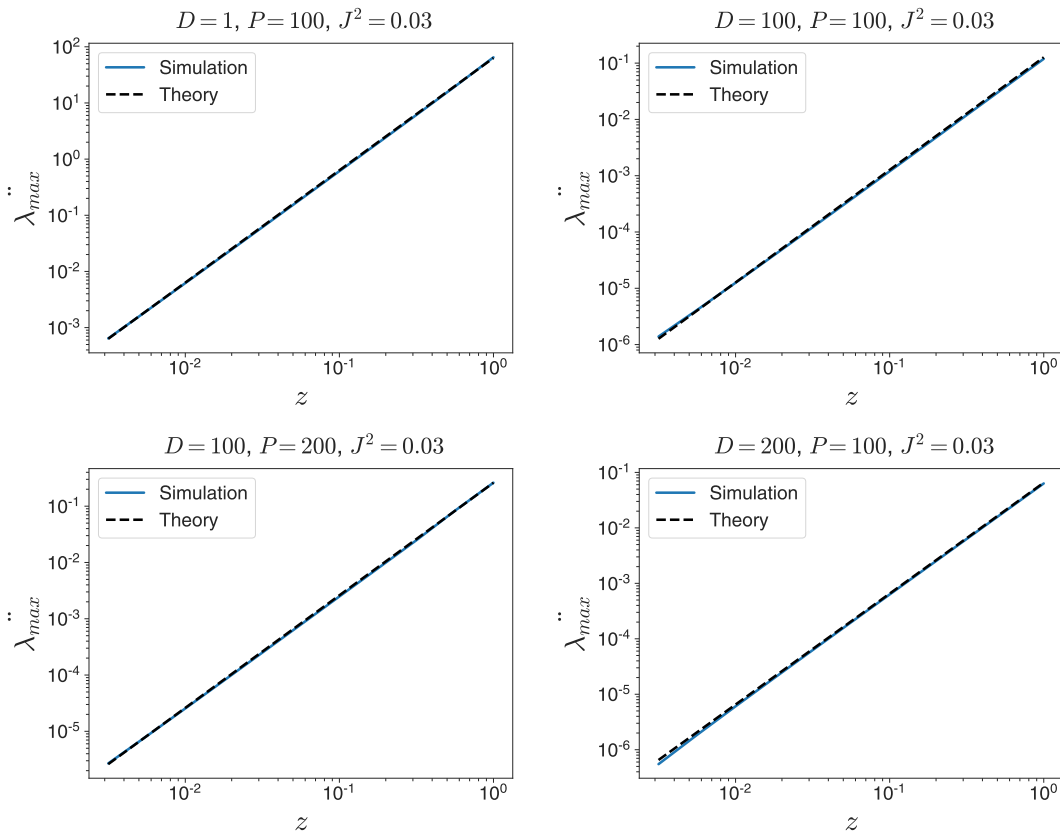


Figure 12. Average $\ddot{\lambda}_{max}(0)$ versus σ_z , various D and P (100 seeds).

This result suggests that as σ_z increases, so does the degree of progressive sharpening. This can be confirmed by looking at GF trajectories (Figure 13). The trajectories with small σ_z don't change their curvature much, and the loss decays exponentially at some rate. However, when σ_z is larger, the curvature increases initially, and then stabilizes to a higher value, allowing for faster convergence to the minimum of the loss.

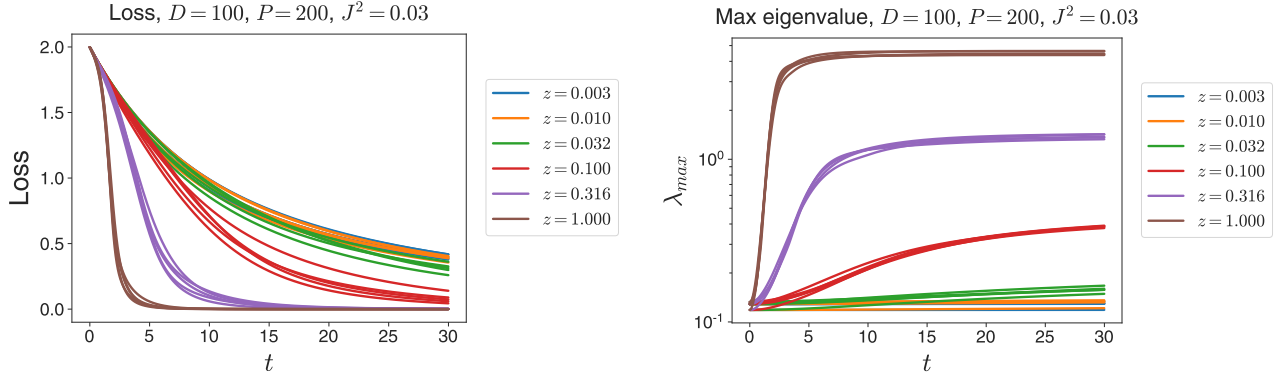


Figure 13. Gradient flow trajectories of loss and max NTK eigenvalues for quadratic regression models for varying σ_z . As σ_z increases, λ_{\max} changes more quickly, and is generally increasing. Models with higher σ_z converge faster in GF dynamics.

C.2. Timescales for gradient descent

Consider a random initialization of \mathbf{z} , \mathbf{J} , and \mathbf{Q} , where the terms are i.i.d. with zero mean variances σ_z^2 , σ_J^2 , and 1 respectively, and finite fourth moments. Furthermore, suppose that \mathbf{z} , \mathbf{J} , and \mathbf{Q} are rotationally invariant in both input and output space. Under these conditions, we hope to compute

$$r_{NL}^2 \equiv \frac{\mathbb{E}[||\frac{1}{2}\eta^2 \mathbf{Q}_{\alpha ij}(\mathbf{J}_{\beta i})_0(\mathbf{z}_\beta)_0(\mathbf{J}_{\delta j})_0(\mathbf{z}_\delta)_0||_2^2]}{\mathbb{E}[||\eta(\mathbf{J}_{\alpha i})_0(\mathbf{J}_{i\beta})_0(\mathbf{z}_\beta)_0||_2^2]} = \frac{1}{4}\eta^2\sigma_z^2D^2 \quad (148)$$

at initialization, in the limit of large D and P .

The denominator is given by:

$$\mathbb{E}[\mathbf{J}_{\alpha i}\mathbf{J}_{\beta i}(\mathbf{z}_\beta)\mathbf{J}_{\alpha j}\mathbf{J}_{\delta j}(\mathbf{z}_\delta)] = \sigma_z^2\mathbb{E}[\mathbf{J}_{\alpha i}\mathbf{J}_{\beta i}\mathbf{J}_{\alpha j}\mathbf{J}_{\delta j}\delta_{\beta\delta}] = \sigma_z^2\mathbb{E}[\mathbf{J}_{\alpha i}\mathbf{J}_{\beta i}\mathbf{J}_{\alpha j}\mathbf{J}_{\beta j}] \quad (149)$$

Evaluation gives us:

$$\mathbb{E}[\mathbf{J}_{\alpha i}\mathbf{J}_{\beta i}(\mathbf{z}_\beta)\mathbf{J}_{\alpha j}\mathbf{J}_{\delta j}(\mathbf{z}_\delta)] = \sigma_z^2(\sigma_J^4(P(P-1)D) + C_4DP) \quad (150)$$

where C_4 is the 4th moment of $\mathbf{J}_{\alpha i}$. To lowest order in D and P

$$\mathbb{E}[\mathbf{J}_{\alpha i}\mathbf{J}_{\beta i}(\mathbf{z}_\beta)\mathbf{J}_{\alpha j}\mathbf{J}_{\delta j}(\mathbf{z}_\delta)] = \sigma_z^2\sigma_J^4DP^2 + O(DP) \quad (151)$$

Evaluating the numerator, we have:

$$\mathbb{E}[\mathbf{Q}_{\alpha ij}\mathbf{J}_{\beta i}\mathbf{z}_\beta\mathbf{J}_{\delta j}\mathbf{z}_\delta\mathbf{Q}_{\alpha mn}\mathbf{J}_{\gamma m}\mathbf{z}_\gamma\mathbf{J}_{\nu n}\mathbf{z}_\nu] = \mathbb{E}[\mathbf{J}_{\beta i}\mathbf{z}_\beta\mathbf{J}_{\delta j}\mathbf{z}_\delta\mathbf{J}_{\gamma m}\mathbf{z}_\gamma\mathbf{J}_{\nu n}\mathbf{z}_\nu](\delta_{im}\delta_{jn} + (M_4 - 1)\delta_{ijmn}) \quad (152)$$

where M_4 is the 4th moment of $\mathbf{Q}_{\alpha ij}$. This gives us:

$$\begin{aligned} \frac{1}{D}\mathbb{E}[\mathbf{Q}_{\alpha ij}\mathbf{J}_{\beta i}\mathbf{z}_\beta\mathbf{J}_{\delta j}\mathbf{z}_\delta\mathbf{Q}_{\alpha mn}\mathbf{J}_{\gamma m}\mathbf{z}_\gamma\mathbf{J}_{\nu n}\mathbf{z}_\nu] &= \mathbb{E}[\mathbf{J}_{\beta i}\mathbf{z}_\beta\mathbf{J}_{\delta j}\mathbf{z}_\delta\mathbf{J}_{\gamma i}\mathbf{z}_\gamma\mathbf{J}_{\nu j}\mathbf{z}_\nu] + \\ &\quad (M_4 - 1)\mathbb{E}[\mathbf{J}_{\beta i}\mathbf{z}_\beta\mathbf{J}_{\delta i}\mathbf{z}_\delta\mathbf{J}_{\gamma i}\mathbf{z}_\gamma\mathbf{J}_{\nu i}\mathbf{z}_\nu] \end{aligned} \quad (153)$$

Next, we perform the \mathbf{z} averages. We have

$$\begin{aligned} \frac{1}{D}\mathbb{E}[\mathbf{Q}_{\alpha ij}\mathbf{J}_{\beta i}\mathbf{z}_\beta\mathbf{J}_{\delta j}\mathbf{z}_\delta\mathbf{Q}_{\alpha mn}\mathbf{J}_{\gamma m}\mathbf{z}_\gamma\mathbf{J}_{\nu n}\mathbf{z}_\nu] &= \sigma_z^4\mathbb{E}[\mathbf{J}_{\beta i}\mathbf{J}_{\delta j}\mathbf{J}_{\gamma i}\mathbf{J}_{\nu j}](\delta_{\beta\delta}\delta_{\gamma\nu} + \delta_{\beta\gamma}\delta_{\delta\nu} + \delta_{\beta\nu}\delta_{\delta\gamma}) \\ &\quad + (C_4 - \sigma^4)\mathbb{E}[\mathbf{J}_{\beta i}\mathbf{J}_{\delta j}\mathbf{J}_{\gamma i}\mathbf{J}_{\nu j}]\delta_{\beta\delta}\delta_{\gamma\nu} \\ &\quad + (M_4 - 1)\sigma_z^4\mathbb{E}[\mathbf{J}_{\beta i}\mathbf{J}_{\delta i}\mathbf{J}_{\gamma i}\mathbf{J}_{\nu i}](\delta_{\beta\delta}\delta_{\gamma\nu} + \delta_{\beta\gamma}\delta_{\delta\nu} + \delta_{\beta\nu}\delta_{\delta\gamma}) \\ &\quad + (M_4 - 1)(C_4 - \sigma^4)\mathbb{E}[\mathbf{J}_{\beta i}\mathbf{J}_{\delta i}\mathbf{J}_{\gamma i}\mathbf{J}_{\nu i}]\delta_{\beta\delta}\delta_{\gamma\nu} \end{aligned} \quad (154)$$

1320 where C_4 is the 4th moment of \mathbf{z} . Simplification gives us:

$$\begin{aligned} 1322 \frac{1}{D} \mathbb{E}[\mathbf{Q}_{\alpha ij} \mathbf{J}_{\beta i} \mathbf{z}_\beta \mathbf{J}_{\delta j} \mathbf{z}_\delta \mathbf{Q}_{\alpha mn} \mathbf{J}_{\gamma m} \mathbf{z}_\gamma \mathbf{J}_{\nu n} \mathbf{z}_\nu] &= \sigma_z^4 (\mathbb{E}[\mathbf{J}_{\beta i} \mathbf{J}_{\beta j} \mathbf{J}_{\delta i} \mathbf{J}_{\delta j}] + \mathbb{E}[\mathbf{J}_{\beta i} \mathbf{J}_{\delta j} \mathbf{J}_{\beta i} \mathbf{J}_{\delta j}] + \mathbb{E}[\mathbf{J}_{\beta i} \mathbf{J}_{\delta j} \mathbf{J}_{\delta i} \mathbf{J}_{\beta j}]) \\ 1323 &\quad + (C_4 - \sigma_z^4) \mathbb{E}[\mathbf{J}_{\beta i} \mathbf{J}_{\beta j} \mathbf{J}_{\beta i} \mathbf{J}_{\beta j}] \\ 1324 &\quad + (M_4 - 1) \sigma_z^4 (\mathbb{E}[\mathbf{J}_{\beta i} \mathbf{J}_{\beta i} \mathbf{J}_{\gamma i} \mathbf{J}_{\gamma i}] + \mathbb{E}[\mathbf{J}_{\beta i} \mathbf{J}_{\delta i} \mathbf{J}_{\beta i} \mathbf{J}_{\delta i}] + \mathbb{E}[\mathbf{J}_{\beta i} \mathbf{J}_{\delta i} \mathbf{J}_{\delta i} \mathbf{J}_{\beta i}]) \\ 1325 &\quad + (M_4 - 1) (C_4 - \sigma_z^4) \mathbb{E}[\mathbf{J}_{\beta i} \mathbf{J}_{\beta i} \mathbf{J}_{\beta i} \mathbf{J}_{\beta i}] \end{aligned} \tag{155}$$

1329 For large D and P , the final three terms are asymptotically smaller than the first term. Evaluating the first term, to leading
1330 order we have:

$$1332 \frac{1}{D} \mathbb{E}[\mathbf{Q}_{\alpha ij} \mathbf{J}_{\beta i} \mathbf{z}_\beta \mathbf{J}_{\delta j} \mathbf{z}_\delta \mathbf{Q}_{\alpha mn} \mathbf{J}_{\gamma m} \mathbf{z}_\gamma \mathbf{J}_{\nu n} \mathbf{z}_\nu] = \sigma_z^4 \sigma_J^4 (2DP^2 + 2D^2P + D^2P^2) + O(D^2P + DP^2) \tag{156}$$

$$1335 \mathbb{E}[\mathbf{Q}_{\alpha ij} \mathbf{J}_{\beta i} \mathbf{z}_\beta \mathbf{J}_{\delta j} \mathbf{z}_\delta \mathbf{Q}_{\alpha mn} \mathbf{J}_{\gamma m} \mathbf{z}_\gamma \mathbf{J}_{\nu n} \mathbf{z}_\nu] = \sigma_z^4 \sigma_J^4 D^3 P^2 + O(D^3 P + D^2 P^2) \tag{157}$$

1337 This gives us:

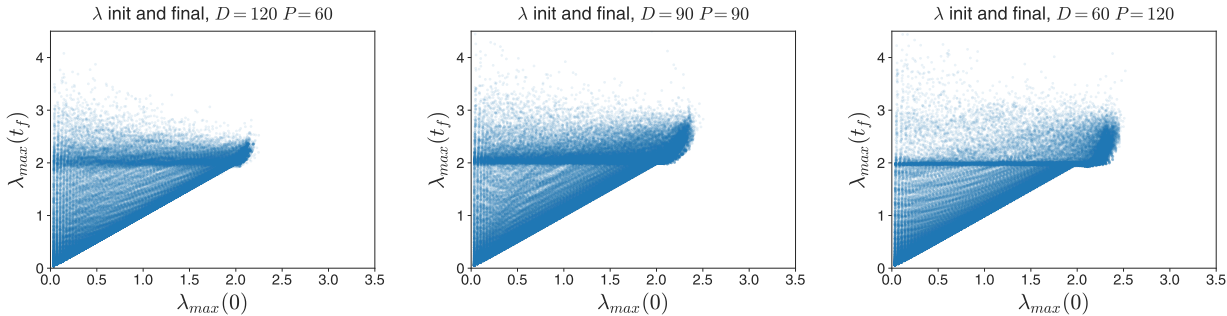
$$1339 r_{NL}^2 = \frac{1}{4} \frac{\sigma_z^4 \sigma_J^4 D^3 P^2}{\sigma_z^2 \sigma_J^4 D P^2} = \frac{1}{4} \sigma_z^2 D^2 \tag{158}$$

1341 to leading order, in the limit of large D and P .

C.3. Dependence on D and P

1345 We can see empirically that the sharpening is more pronounced in the overparameterized regime where $D > P$. Using
1346 the trajectories from Figure 4, we can make a scatter plot of the normalized maximum NTK eigenvalues $\eta \lambda_{max}$ at both
1347 initialization and the final point of the dynamics (Figure 14). In all cases, a variety of initializations (x-axis) lead to final
1348 values which concentrate around 2 (y-axis).

1349 We can see that the concentration is tightest for the overparameterized regime where $P > D$ (right plot). We hypothesize
1350 that for large D and P , the EOS behavior is stronger and more likely to happen when $P > D$. We leave further exploration
1351 of this hypothesis for future work.



1364 *Figure 14.* Scatter plots of initial vs. final normalized maximum eigenvalues $\eta \lambda_{max}$ for quadratic regression models. Trajectories are
1365 taken from the data used to generate Figure 4. For large D and P , as the model becomes overparameterized ($P > D$), a subset of
1366 trajectories show tighter EOS behavior where $\eta \lambda_{max}$ concentrates close to 2 for a variety of initializations.

D. Analysis of real models

D.1. Experimental setup

1372 The experiments in Section 5 were designed following the setup of Cohen et al. (2022a). We trained a two-hidden layer fully
1373 connected network with tanh non-linearity and hidden dimension 200 on the first 5000 samples of 10 class CIFAR10.
1374

1375 We computed the spectra of the NTK, the loss Hessian, and \mathbf{Q} using a Lanczos method (Ghorbani et al., 2019). We used
 1376 order 36 for both the NTK and \mathbf{Q} , and order 50 for the loss Hessian. All experiments were conducted on GPU with
 1377 float32 precision.

1378

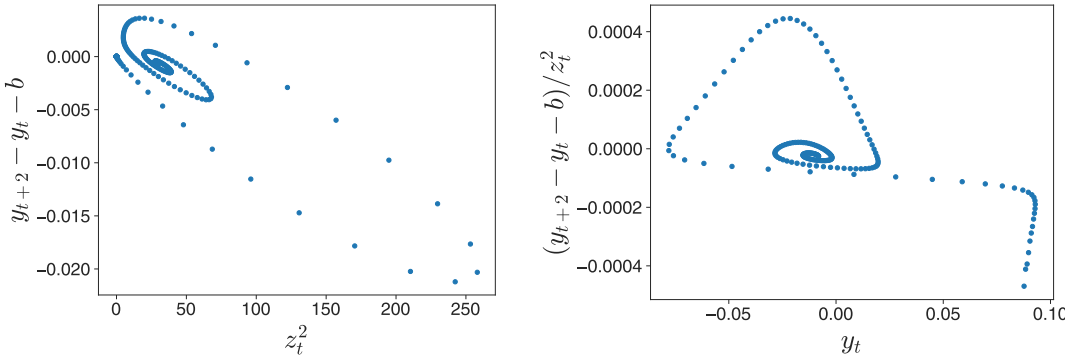
1379 **D.2. Dynamics of y in CIFAR10 model**

1380

1381 The dynamics of y in the CIFAR10 model analyzed in Section 5 are more complicated than the z_1 dynamics. We see from
 1382 Figure 5 that there is a z_1 and y -independent component of the two-step change in y . We can approximate this change b by
 1383 computing the average value of $y_{t+2} - y_t$ for small z_1 (taking $z_1 < 10^{-4}$ in this case). We can then subtract off b from
 1384 $y_{t+2} - y_t$, and plot the remainder against z_t^2 (Figure 15 left). We see that $y_{t+2} - y_t - b$ is negatively correlated with z_t^2 ,
 1385 particularly for large z_t . However, $y_{t+2} - y_t$ is clearly not simply function of z_1 .

1386 The two-step model dynamics could be written as $(ay + c)z^2$. If we plot $(y_{t+2} - y_t - b)/z_t^2$ versus y_t , we again don't have
 1387 a single-valued function (Figure 15, right). Therefore, the functional form of $y_{t+2} - y_t$ is not given by $b + ayz_1^2 + cz_1^2$.

1388



1401 *Figure 15.* Gradient flow trajectories of loss and max NTK eigenvalues for quadratic regression models for varying σ_z . As σ_z increases,
 1402 λ_{\max} changes more quickly, and is generally increasing. Models with higher σ_z converge faster in GF dynamics.

1403

1404 **D.3. Quadratic expansion of 2-class CIFAR model**

1405

We trained a CIFAR model using the first two classes only with 5000 datapoints using the Neural Tangents library (Novak et al., 2019) - which let us perform 2nd and 3rd order Taylor expansions of the model at arbitrary parameters. The models were 2-hidden layer fully-connected networks, with hidden width 256 and Erf non-linearities. Models were initialized with the NTK parameterization, with weight variance 1 and bias variance 0. The targets were scalar valued - +1 for the first class, -1 for the second class. A learning rate of 0.003204 was used in all experiments. All plots were made using float-64 precision.

Taking a quadratic expansion at initialization, we see that the loss tracks the full model for the first 1000 steps in this setting (Figure 16, left), but misses the edge-of-stability behavior. We use Neural Tangents to efficiently compute the NTK to get the top eigenvalue λ_1 (and consequently, y). We can also compute z_1 by computing the associated eigenvector \mathbf{v}_1 and projecting residuals \mathbf{z} . If the quadratic expansion is taken closer to the edge of stability, the dynamics of z_1 well approximates the true z_1 dynamics, up to a shift associated with exponential growth of z_1 occurring at different times (Figure 16, middle). We see that the shape of the first peak in $|z_1|$ is the same for the full model and the quadratic model, but the subsequent oscillations are faster and more quickly damped in the full model. This suggests that the initial EOS behavior may be captured by the quadratic model, but the detailed dynamics require an understanding of higher order terms. For example, the 3rd order Taylor expansion improves the prediction of the magnitude and period of the oscillations, but still misses key quantitative features (Figure 16, right).

1423

1424

1425

1426

1427

1428

1429

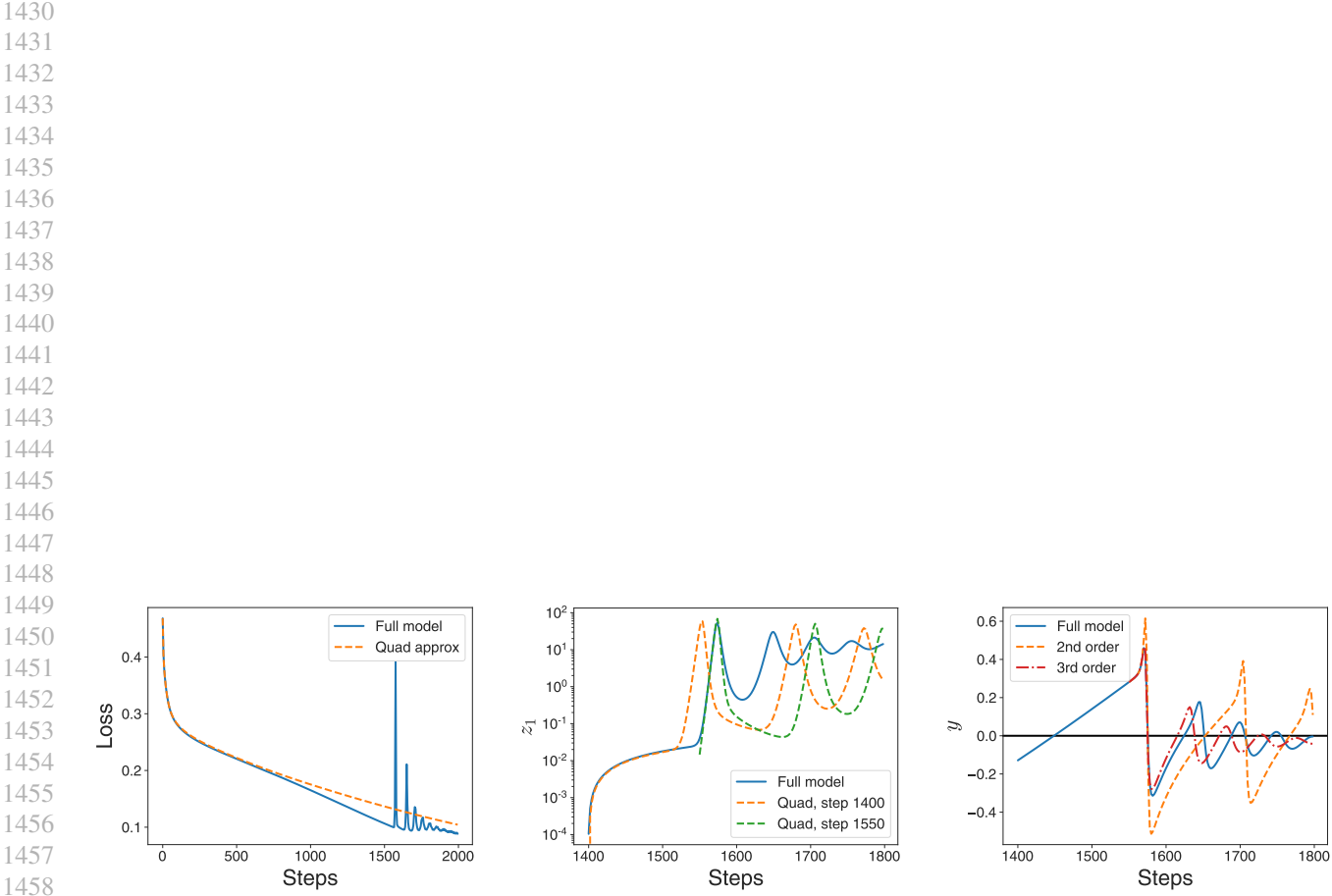


Figure 16. Quadratic expansion of FCN model trained on two-class CIFAR. Expanding at initialization gives good approximation to full model for 1000 steps, after which EOS behavior occurs in full model but not approximate one (left). When z_1 is small, quadratic model tracks full model; however, initial exponential increase may happen earlier in approximate model (middle). Magnitude of z_1 has larger oscillations in full model compared to approximate model. Third-order Taylor expansion better captures magnitude and period of oscillations, but still misses quantitative features (right).